The American Monsoon System in HadGEM3.0 and UKESM1 CMIP6 simulations

Jorge L. García-Franco[1], Lesley J. Gray[1,2], and Scott Osprey[1,2]

[1]Atmospheric, Oceanic and Planetary Physics, Department of Physics. University of Oxford.
[2]National Centre for Atmospheric Science, UK.

Correspondence: Jorge L García-Franco: jorge.garcia-franco@physics.ox.ac.uk

Abstract. The simulated climate in the American Monsoon System (AMS) in the CMIP6 submissions of HadGEM3.0 GC3.1 and the UKESM1 is assessed and compared to observations and reanalysis. Pre-industrial control and historical experiments are analysed to evaluate the model representation of this monsoon under different configurations, resolutions and with and without Earth System processes. The simulations exhibit a good representation of the temperature and precipitation seasonal

5 cycles, although the historical experiments overestimate summer temperature in the Amazon, Mexico and Central America by more than 1.5 K. The seasonal cycle of rainfall and general characteristics of the North American Monsoon are well represented by all the simulations. The models simulate the bimodal regime of precipitation in southern Mexico, Central America and the Caribbean known as the midsummer drought, although with a stronger intraseasonal variation than observed. Austral summer biases in the modelled Atlantic Intertropical Convergence Zone (ITCZ), Walker Circulation, cloud cover

10 and regional temperature distributions are significant and influenced the simulated spatial distribution of rainfall in the South American Monsoon. These biases lead to an overestimation of precipitation in southeastern Brazil and an underestimation of precipitation in the Amazon. El Niño Southern Oscillation (ENSO) characteristics and teleconnections to the AMS are well represented by the simulations. The precipitation responses to the positive and negative phase of ENSO in subtropical America are linear in both pre-industrial and historical experiments. Overall, the UKESM has the same performance as the

15 lower resolution simulation of HadGEM3.0 GC3.1 and no significant difference for the AMS was found between the two model configurations. In contrast, the medium resolution HadGEM3.0 GC3.1 N216 simulation outperforms the low-resolution simulations in temperature, rainfall, ITCZ and Walker circulation biases.

Copyright statement. TEXT

1 Introduction

20 The American Monsoon System (AMS) is the regional monsoon associated with summer rainfall in subtropical North and South America. The AMS is largely the copuled rainfall and circulation response to the seasonal migration of the Intertropical Convergence Zone (ITCZ) around subtropical America (Zhou et al., 2016), and is is typically subdivided into the North and

South American Monsoon Systems (Vera et al., 2006). Although rainfall in southern Mexico and Central America is not formally part of a monsoon system, precipitation in this region follows a strong seasonal cycle and is intrinsically linked to the ITCZ. For this resason, some aspects of Central American rainfall have been analysed as a part of the AMS (e.g Vera et al., 2006; Wang et al., 2017; Pascale et al., 2019).

The North American Monsoon is the northernmost part of the AMS and the main source of rainfall in south-western North America, with the core region located in northwestern Mexico (Adams and Comrie, 1997; Stensrud et al., 1997; Vera et al., 2006). The seasonal cycle is characterised by a wet July-August-September season and significantly drier conditions during the rest of the year (Adams and Comrie, 1997). Several features of the North American Monsoon are modulated by factors associated with the East Pacific Ocean or the Gulf of Mexico, e.g., the tracks of inverted troughs or the frequency of Gulf Surges (Douglas et al., 1993; Adams and Comrie, 1997; Seastrand et al., 2015; Lahmers et al., 2016). Moisture in the North American Monsoon is mainly advected in the low-level flow from the Gulf of California and the East Pacific Ocean whereas moisture mixed in the mid-troposphere from the Caribbean Sea and Gulf of Mexico is a secondary, but relevant, source (e.g Stensrud et al., 1997; Pascale and Bordoni, 2016; Ordoñez et al., 2019).

A bimodal regime characterises the seasonal cycle of precipitation in southern Mexico, Central America and the Caribbean that is typically referred to as Midsummer Drought (MSD) (Magaña et al., 1999; Gamble et al., 2008). In southern Mexico and northern Central America, the seasonal cycle is characterised by two precipitation maxima, in June and September, that are separated by a decrease in precipitation during July and August. The mechanisms underpinning the intraseasonal variations of rainfall have been associated with features such as the Caribbean Low-Level Jet, the North Atlantic Subtropical High and the East Pacific Sea-Surface Temperatures (SSTs) (e.g Gamble et al., 2008; Yin et al., 2013; Herrera et al., 2015). The complex interplay of moisture transport, evaporation and the dynamics the features largely characterise the MSD characteristics, which makes it a challenge for climate models to reproduce accurately all the relevant features for rainfall in this region (Ryu and Hayhoe, 2014).

The South American Monsoon is a primary source of precipitation for South America, especially in the Amazon region (Gan et al., 2004; Vera et al., 2006; Jones and Carvalho, 2013). During austral summer (DJF) monsoon rainfall accounts for over 60% of the total annual precipitation in the Amazon (Gan et al., 2004; Marengo et al., 2012), whereas austral winter rainfall accounts for less than 5% of the total annual precipitation in some regions (Vera et al., 2006). The spatial domain of the South American Monsoon generally includes central and southeastern Brazil, Bolivia, northern Argentina and Paraguay but this definition can vary amongst studies (e.g. Jones and Carvalho, 2002; Bombardi and Carvalho, 2011; Marengo et al., 2012; Yin et al., 2013). The date of monsoon onset is also region-dependent; in northern South-America convection is observed from early October, whereas convection in southeastern Brazil typically starts in mid-November or later (Marengo et al., 2001; Nieto-Ferreira and Rickenbach, 2011). The mean-state and variability of the Atlantic, in particular the SSTs and the Intertropical Convergence Zone (ITCZ), greatly influences the South American Monsoon, as demonstrated in observations and climate models (see e.g. Giannini et al., 2004; Vera and Silvestri, 2009; Lee et al., 2011).

General Circulation Models (GCMs) have been used to improve our understanding of the AMS climate, particularly to understand the current and future effect of greenhouse forcing on the characteristics of monsoon rainfall (see e.g. Arritt et al.,

2000; Sheffield et al., 2013a; Geil et al., 2013; Ryu and Hayhoe, 2014; Seager and Vecchi, 2010; Colorado-Ruiz et al., 2018).
Modelling studies have also assesed how horizontal resolution modifies the simulated climate (Pascale et al., 2016) and how

60   climatological model biases affect simulated teleconnections (Vera and Silvestri, 2009; Bayr et al., 2019). The climate mod-
elling intercomparison project (CMIP5) historical experiments showed model improvements with respect to previous MIPs,
particularly in seasonal features (Geil et al., 2013; Sheffield et al., 2013a; Ryu and Hayhoe, 2014). However, CMIP5 models in
the North American Monsoon misrepresented the magnitude of the monthly-mean seasonal cycle of precipitation and exhibited
a later than observed retreat date (Geil et al., 2013; Sheffield et al., 2013a). In MSD regions, most of these experiments were

65   unable to represent the seasonal cycle of the MSD and the total annual rainfall in Central America and the Caribbean; however,
some models such as those from the MetOffice Hadley Centre reasonably simulated the observed bimodal regime (Ryu and
Hayhoe, 2014). For the South American Monsoon, CMIP5 models improved the simulated distribution of precipitation during
monsoon maturity and exhibited an improved seasonal cycle (Jones and Carvalho, 2013; Yin et al., 2013). However, rain-
fall during the fall season and the South Atlantic Convergence Zone were poorly represented. Overall, very few studies have

70   analysed the relative roles of large-scale biases for monsoon representation or the links between features such as the ITCZ or
the Walker circulation and the AMS, which may be particularly important when understanding projected responses to forcing
(Zhou et al., 2016; Wang et al., 2017).

The next efforts to improve climate models include increased horizontal resolution, better parameterisations and/or the
addition of processes in new models known as Earth System models (Eyring et al., 2016). The comparison and evaluation of

75   simulations with increased horizontal resolution and Earth System models may suggest where modelling efforts are resulting in
significant improvements in model skill. This comparison may be relevant when interpreting scenario results and projections,
which often require statistical methods to select the best models to make an ensemble-mean projection into future climate
(see e.g. Colorado-Ruiz et al., 2018). This study analyses the output from the two Met Office Hadley Centre (MOHC) models
including three pre-industrial control and two historical experiments submitted to the Climate Modelling Intercomparison

80   Project Phase 6 (CMIP6) (Eyring et al., 2016). The MOHC models have typically performed above average in and around the
AMS (e.g. Jones and Carvalho, 2013; Geil et al., 2013).

The main purpose of this paper is to validate the UKESM1, an Earth System model, and HadGEM3.1, the latest generation
of the Hadley Centre Global Environment model in their representation of the AMS. The study documents the main biases
in the simulated climate of UKESM1 and HadGEM3.0 and compares the effect of increased horizontal resolution and Earth

85   System processes on the representation of the AMS climate. The analysis provides a framework for using these climate models
in scenario studies, to highlight possible sources of model error that may be corrected and to further understand variability
and teleconnections in this region. The remainder of this paper is organised as follows: section 2 describes the observations,
reanalyses and models used, section 3 compares modelled and observed climatological features such as the Walker circula-
tion. Section 4 analyses the characteristics of rainfall and convection in the AMS while section 5 documents the simulated

90   teleconnections of ENSO. Section 6 provides a summary and discussion.

Table 1. Summary of the datasets used in this study. For each dataset, the acronym used hereafter, the period of coverage, the field used and the horizontal resolution are shown. Some datasets extend further back in time, but only the satellite-era period is used in most of the datasets. The variables used are: precipitation, surface temperature ($Tsurf$), sea-level pressure (SLP), SSTs, the x and y components of the wind (u, v), the lagrangian tendency of air pressure (ω), outgoing longwave radiation (OLR) and specific humidity (q).

Dataset/ Version	Acronym	Variable	Period	Data type	Resolution	Reference
Global Precipitation Climatology Project v2.3	GPCP	Precipitation	(1979-2018)	Surface station and satellite	2.5°x2.5°	(Adler et al., 2003)
Global Precipitation Climatology Centre	GPCC	Precipitation	(1940-2013)	Surface station	0.5°x0.5°	(Becker et al., 2011)
Climatic Research Unit TS v4.	CRU4	Surface temperature	(1979-2017)	Surface station	0.5°x0.5°	(Harris et al., 2014)
Climate Hazards Infrared Precipitation with Stations	CHIRPS	Precipitation	(1981-2018)	Surface station and satellite	0.05°x0.05°	(Funk et al., 2015)
Tropical Rainfall Measurement Mission	TRMM	Precipitation	(1999-2018)	Surface station and satellite	0.25°x0.25°	(Huffman et al., 2010)
Hadley Centre SST3	HadSST	SST	(1940-2018)	Buoy and satellite	2.5°x2.5°	(Kennedy et al., 2011)
European Centre for Medium-Range Forecasting ERA-5	ERA-5	$Tsurf$, SLP, u, v, ω, OLR, q	(1979-2018)	Reanalysis	0.75x0.75°	(C3S, 2017)

2 Data and methods

We use several observational and reanalysis datasets to validate the simulations. Table 1 summarises relevant information of the observations and reanalysis datasets used in this study. In short, surface and satellite observations were used where available, whereas other metrics were taken from reanalysis data from the European Centre for Medium-Range Weather Forecasts

95 (ECMWF): ERA-5, downloaded from https://climate.copernicus.eu/climate-reanalysis. Four different precipitation datasets are used; although TRMM provides the most reliable source of information about the horizontal and temporal distribution of rainfall, the period covered by TRMM is too short (1998-2018) to, for example, analyse statistically robust teleconnections. GPCP, GPCC and CHIRPS are also used for their longer period, although arguably each of these datasets have shortcomings in either resolution or spatial coverage.

100 ### 2.1 Model data

The MOHC has submitted the output of two models for CMIP6: HadGEM3.0 GC3.1 and UKESM1. HadGEM3.0 GC3.1 (hereafter GC3) is the latest version of the Global Coupled (GC) MetOffice Unified Model (UM). The most substantial change

from the version used in CMIP5 (HadGEM2-AO) is the inclusion of the new GC configuration 3.1 which includes the following components: Global Atmosphere 7.0 (GA7.0), Global Land 7.0 (GL7.0), Global Ocean 6.0 (GO6.0), and Global Sea Ice

105 8.0 (GSI8.0). The GC3.1 configuration runs with 85 atmospheric levels, 4 soil levels and 75 ocean levels and is extensively described in Williams et al. (2018).

The UKESM1 is a new Earth System Model that aims to improve climate representation by resolving additional processes of the Earth System. These additional components include marine chemical and biological processes, improved air-soil and aerosol-chemistry interactions, as well as dynamic vegetation (Mulcahy et al., 2018; Sellar et al., 2019). The phys-

110 ical atmosphere-land-ocean-sea-ice core of the HadGEM3.0 GC3.1 underpins the UKESM1, so that the UKESM1 and the HadGEM3.0 have the same dynamical core (same ocean, atmosphere and land-surface levels, convection schemes, etc.) but the UKESM1 has the additional components mentioned above.

The piControl simulations of GC3 were run using two horizontal resolutions: 1.875°x 1.25° (N96) and 0.83°x 0.56° (N216) (Menary et al., 2018), which correspond to approximately 135 and 65 km at midlatitudes, respectively. The piControl simu-

115 lation of UKESM1 was run at the same resolution as GC3 N96-pi, which means that UKESM1-pi can be compared directly with GC3 N96-pi to evaluate the effect of the Earth System processes on the simulated climate without external forcing. In this study, 500 years of the piControl simulations are used for the monthly mean analysis and 300 years for the analyses on shorter time-scales.

The historical experiments are 164-yr integrations beginning for 1850-2014 that include historical forcings that include

120 aerosol, greenhouse gas, volcanic and solar signals since 1850 (Eyring et al., 2016; Andrews et al., 2019), and can therefore be directly compared to observations. The historical experiments of HadGEM3 and UKESM1 are composed of ensembles with 4 and 9 ensemble members, respectively. The results for the historical experiment will typically be presented as the ensemble mean for spatial distributions or with the ensemble spread for seasonal cycles. These experiments will be referred to as GC3-hist and UKESM1-hist hereafter.

125 3 Climatological features

This section compares the simulated climatological temperature and low-level wind structure in the AMS region over different seasons, as well as several characteristics of the ITCZ and the Walker circulation, with reanalysis data.

3.1 Temperature and low-level winds

The climatological representation of the surface temperature and low-level winds in the models is compared to ERA5 in Figures

130 1 and 2. First, the climatology of DJF and JJA of ERA5 is shown in Figure 1a, b. The biases of the historical experiments, computed as the differences between the model and observed fields, are shown in Figures 1c, d) for GC3-hist and e, f) for UKESM1-hist. Only statistically significant differences are shown, according to a Welch t-test. During DJF, the simulations show a colder-than-observed sub-tropical North America and a warm bias over South America which maximizes in the Amazon (≈ 3.5 K). The west coast of South America also shows a significant positive bias of over 4 K. The simulated circulation in

135   austral summer in South America has a significant bias in the easterly flow coming from the equatorial and subtropical Atlantic. The biases in the low-level winds suggest a weaker easterly flow into southeastern Brazil but also a strong southward flow from northern to southern South America. For example, the Bolivian Low-Level Jet, which is the strong southward flow observed in Figure 1a in Bolivia, is stronger in the simulations.

During boreal summer (Figures 1d, f), positive biases are found in southwestern North America (> 3.5 K), which are higher
140   in UKESM1-hist than in GC3-hist. The flow in the western coast of Central America has a bias in UKESM1 in the easterly flow that crosses from the Caribbean Sea into the East Pacific Ocean. Both models show an anticyclonic anomaly in the region of the North Atlantic Subtropical High. Also in JJA, the simulated East Pacific surface temperature are colder than observed for both historical experiments.

Figure 2 compares the GC3 piControl simulations with ERA5 and also with their respective historical experiments. In DJF,
145   the piControl simulations show a positive bias in the Amazon, just as in the historical experiments, although smaller and a similar bias in the circulation in South America, particularly for GC3 N96-pi. The South American low-level circulation of GC3 N216-pi has the smallest biases with respect to ERA5 amongst all the simualtions. UKESM1-pi was found to be almost indistinguishable from GC3 N96-pi, which is why in this and the following sections only GC3 N96-pi results are shown. Figure 2e, f show the difference between the historical and piControl experiment of GC3, which illustrates the response to historical
150   forcing in GC3. This temperature response in South and Central America was of about 1.5 K whereas in JJA in North America, temperatures were 4 K higher in the historical experiment than in the piControl. A very similar temperature pattern response to historical forcing was observed for UKESM1 (not shown) although of slightly different magnitude. The only dynamical response to forcing seems to be the easterlies in the East Pacific Ocean during JJA.

The seasonal evolution of temperature in key regions of the AMS is shown in Figure 3 which provides a better comparison
155   of the temperature field in these experiments. The strongest seasonal contrast in surface temperature is in the North American Monsoon region, where wintertime temperatures are roughly 12°C and June temperatures are close to 27°C. Although colder than observed in the piControl and warmer in the historical experiments throughout the whole year, the models accurately reproduce the seasonal cycle of this region, which may be relevant for the simulated onset timing and strength of the monsoon (Turrent and Cavazos, 2009).

160   The piControls show a colder-than-observed winter in southern Mexico and northern Central America whereas the historical experiments show a warming signal of about 1.5 K in winter and 2 K in the summer when compared to the piControls. In spite of these biases, both types of experiments follow closely the seasonal cycle in North and Central America. However, the temperature cycle in South America is poorly represented in the simulations (Figures 3 c, d). The models seem to reproduce a stronger than observed seasonal cycle, as observed by the 4 K temperature difference between late austral winter and spring,
165   whereas the annual cycle of temperature varies by less than 1 K in the observations. The warmer than observed Amazon (Fig. 3 d) bias peaks in austral spring (SON), during the development of the monsoon (Marengo et al., 2012). In southeastern Brazil, the seasonal cycle is reasonably well reproduced but with a significant cold bias throughout the year which is significantly larger during austral winter (JJA), as models (e.g. UKESM1) simulate a temperature of 292 K which is 4 K lower than the

observed 296 K. In all panels of Figure 3, the historical experiments show a larger warming signal as a response to forcing in
170 UKESM1 than in GC3.

3.2 The ITCZ and the Walker circulation

The AMS is intertwined with the seasonal migration of the East Pacific and Atlantic ITCZ and associated with the Walker
circulation through teleconnections (Zhou et al., 2016). This section validates the modelled ITCZs and Walker circulation.

Figure 4 shows the observed and modelled climatological rainfall and the ITCZ climatological position in the East Pacific
175 and Atlantic Oceans. Three simulations are shown: the ensemble-mean UKESM1-historical, GC3 N96-pi and GC3 N216-pi.
We choose this set of simulations because the simulations of lower resolution, both historical and piControl, showed very
similar ITCZ characteristics, as will be described below, and relatively few differences were found across, e.g., GC3 N96-pi
and GC3-hist.

The observed ITCZ (Figure 4a) is found, on average, at 8°N in the East Pacific and at 6°N in the Atlantic. All the simulations
180 reasonably represent the climatological position of the East Pacific ITCZ; however, the modelled Atlantic ITCZ near the coast
of Brazil is found south of the equator at 3°S. The GC3 N216-pi ITCZ is more consistent with the climatological position
of the ITCZ and rainfall distribution of the TRMM dataset, although stronger-than-observed precipitation is still found south
of the equatorial Atlantic. In the central Pacific, south of the equator at 10°S, all models exhibit a significant positive bias in
rainfall. For instance, consider rainfall in the region of [170°W, 10°S] which in models is found to be above 10 mm day^{-1},
185 yet the observed rainfall is 6 mm day^{-1}. Similarly, rainfall of the easternmost coast of Brazil is significantly larger in all the
simulations than in the TRMM dataset.

The seasonal cycle of the ITCZ, precipitation rates and low-level winds in both basins are shown in Figure 5, for TRMM and
the same three simulations as before. The East Pacific ITCZ in observations (Fig. 5a) migrates southwards during the first days
of the year until the ITCZ reaches a minimum latitude of 5°N around day 100 (mid-April) while also reaching a minimum in
190 precipitation. Afterwards, the ITCZ migrates northward reaching a peak latitude and mean rainfall at 10°N by day 250, or May
30. The low-level winds are predominantly easterlies, which are stronger away from the ITCZ and weaker and convergent near
the ITCZ position. The position and seasonal migration of the East Pacific ITCZ is reasonably well represented in the three
simulations (Figs. 5b, d, e) but the modelled low-level wind structure shows significant biases near the ITCZ.

The observed Atlantic ITCZ (Figure 5b) has a similar seasonal cycle to the East Pacific ITCZ. The Atlantic ITCZ is close to
195 4°N at day 1 and migrates south at the start of the year reaching a minimum of roughly 0° at the end of March, with significant
precipitation south of the equator. During boreal spring, the Atlantic ITCZ migrates north, reaching 8°N at the start of boreal
summer. The boreal winter position of the modelled ITCZs is displaced with respect to the observations. The simulated ITCZ
crosses south of the equator during boreal winter to a region with rainrates above 12 mm day^{-1} that are found between 10-0°S.
After boreal spring, the modelled ITCZ crosses back north of the equator and matches the observed ITCZ reasonably well for
200 boreal summer and fall.

Low-level wind biases are also found near the ITCZ, for instance, between days 1 and 100, Figures 5f and h show that north
of the equator the models show a stronger than observed northward wind, and a stronger than normal southward wind south of

10°S. These biases in the wind flow as well as the ITCZ biases described above were found to be of similar magnitude in the simulations run at N96 resolution, both historical and piControl experiments, however, these biases improved in the medium

205   resolution GC3 N216-pi.

The Walker circulation influences the AMS via the modulation of ascending and descending motions in the eastern Pacific Ocean. These motions affect the upper-level tropical atmosphere connecting the tropical basins (Zhou et al., 2016; Cai et al., 2019). Figures 6a, b show the Walker circulation during boreal winter in ERA5 as diagnosed by zonal and vertical velocities, and specific humidity in the latitude bands of 0-5°N and 5-0°S.

210   The biases are shown in Figures 6c-h for the same set of simulations as for the ITCZ. Significant biases in vertical velocity are found in the Indian and west Pacific Oceans, particularly in the low resolution simulations. Positive vertical velocity biases in the west Pacific Ocean are found north of the equator whereas the positive biases in the Indian Ocean are found south of the equator. Negative ω and low-level moisture biases in central and East Pacific Oceans are also significant in the GC3-N96-pi both north and south of the equator. Around equatorial South America (longitudes 280-310°) there are also significant negative

215   vertical velocity and specific humidity (q) biases north and south of the equator. For example, the UKESM1-hist biases (Figure 6c, d) show a simulated weaker ascent north and south of the equator in this region. The Atlantic Ocean shows anomalously strong ascent south of the equator and anomalously weak ascent north of the equator in the low resolution simulations (Figures 6c, d, e, f). Most of the biases in ω and specific humidity are smaller in the GC3 N216-pi simulation.

The largest biases in zonal wind in the lower resolution simulations are found in the upper troposphere in the East Pacific

220   Ocean and over South America. These are observed as negative zonal wind biases, indicative of significantly weaker upper-level westerlies resulting from the overturning circulation in the Pacific Ocean. The biases in zonal wind of the higher resolution simulation (GC3 N216-pi - Figure 6g, h) are smaller than the biases of the lower resolution simulations.

4 The American Monsoon System

This section compares the spatial and temporal distribution of rainfall in four key regions of the AMS between observations

225   and reanalysis, and the simulations, as well as other characteristics of convective activity, such as height and strength.

4.1 Mean seasonal precipitation

The austral summer (DJF) rainfall distribution and biases in South America are shown in Figure 7. Figure 7a shows the distribution of rainfall in TRMM where rainfall maxima is found in the core Amazon region and along the Andes cordillera. A region with considerable rainfall spreads from the Amazon into south-eastern Brazil and into the south Atlantic Ocean

230   associated with the South Atlantic Convergence Zone (Carvalho et al., 2004).

The low resolution simulations (Figures 7b, c) overestimate rainfall in southeastern Brazil and underestimate rainfall in the core Amazon region. The biases are best illustrated by Figures 7e, g as the difference between the simulations and TRMM. These low resolution simulations show three relevant biases. First, an Atlantic ITCZ displaced to the south, observed as positive (+5 mm day^{-1}) differences south of the equator and negative differences (-5 mm day^{-1}) north of the equator in the Atlantic

Ocean. Second, the models underestimate rainfall in the core Amazon basin by -3 mm day^{-1} on average, whereas rainfall in southeastern Brazil is overestimated by more than +5 mm day^{-1}, which is close to 100% of the observed rainfall in this region. The magnitude of these biases decreases in GC3 N216 (Figure 7f) but the spatial structure described above is similar. The response to historical forcing, illustrated by the difference between UKESM1-hist and UKESM1-pi (Figure 7h), is much weaker than the magnitude of the biases. The AMIP simulations (not shown) removed the spatial patterns of these biases significantly, highlighting the importance of Atlantic SST biases for the representation of the South American Monsoon.

The modelled and observed JJA mean rainfall and biases for southern North and Central America are shown in Figure 8. The dominant feature in the observations (Figure 8a) is the East Pacific ITCZ which extends north to 15°N near the western coast of Mexico as a broad band where mean rainfall exceeds 11 mm day^{-1}. The North American Monsoon can be observed as a band of significant rainfall across western Mexico and southwestern US. In the core monsoon region, near the Sierra Madre Occidental (Adams and Comrie, 1997; Zhou et al., 2016), the mean summer rainfall is higher than 6 mm day^{-1}.

The biases shown in Figures 8e, f, g show that the modelled East Pacific ITCZ rainfall near the western coast of Central America is overestimated by more than 5 mm day^{-1}. This positive bias extends to southern Central America. The low-resolution simulations also show a large underestimation of rainfall (-5 mm day^{-1}) over land in southern Mexico, Guatemala and Belize. Rainfall in the Caribbean islands and southern Florida is slightly underestimated (-1 mm day^{-1}) in all simulations. The distribution of rainfall in the North American Monsoon region is fairly well represented in all the simulations; however, all the simulations overestimate rainfall in the southern part, or the Mexican part of the monsoon by more than 2 mm day^{-1}. The extent of the North American Monsoon to southwestern US is best represented by the high resolution simulation GC3 N216-pi. In most cases, the biases were reduced in the high-resolution simulation (Figure 8f). As for the South American Monsoon, the response to historical forcing is orders of magnitude lower than the biases (Figure 8h) but the overall signal of historical forcing is of drying. In this region, the AMIP simulations showed no significant improvement (not shown).

4.2 The annual cycle of rainfall

Figure 9 shows the pentad-mean cycle of rainfall over the North American Monsoon, the Midsummer drought (MSD), the Amazon Basin and Eastern Brazil regions. The seasonal cycle of precipitation in the MSD region in the simulations is well represented as they show the characteristic bimodal distribution. However, the characteristics of the seasonal cycle in the simulations are different to observations. For example, the magnitude of the first peak in the simulations is higher than TRMM by 2-4 mm day^{-1} and similarly, the variations from first to second peak are more pronounced in the models.

Rainfall in the North American Monsoon has an onset date of around June 14 (Geil et al., 2013), which can observed in the TRMM and CHIRPS datasets in Figure 9b. The three simulations show a sharp increase of rainfall around a similar date, suggesting that onset timing and strength is well represented in these models. Moreover, the modelled and the observed average rainfall during monsoon maturity is 4 mm day^{-1}, found from mid-July until early September. The timing of monsoon retreat is also well represented by the simulations, as both modelled and observed rainfall decay during September. However, the historical simulations show a slightly sooner than observed retreat, by about 2 pentads. For instance, GC3-hist retreats on

average around August 16th. However, winter-time rainfall, before monsoon onset and after monsoon retreat, is overestimated by all the simulations, particularly the higher resolution GC3.1 N216 which has a positive bias of 2 mm day^{-1} in early winter.

270   The strong monsoonal seasonal cycle of precipitation in eastern Brazil is characterised by a very wet summer ($\sim$8 mm day^{-1}) compared to a very dry ($\sim$0.2 mm day^{-1}) winter. The austral summer rainfall in the observations consistently shows that maximum rainfall is found in early January ($\sim$8 mm day^{-1}). Rainfall in this region decreases to $\sim$6 mm day^{-1} by late March as the monsoon migrates northward, to then, sharply descend in austral fall (April). The models (Figure 9c) show a positive bias at the peak stage of the monsoonal rainfall. This bias was found to be of +4 mm day^{-1} and +2.5 mm day^{-1} for

275   the low and high resolution simulations, respectively. The bias in the seasonal cycle is consistent with the seasonal mean bias shown in Figure 7, which showed that rainfall in southeastern Brazil is overestimated in all the simulations, but this bias is smaller in the GC3 N216-pi simulation. In spite of this positive bias in the magnitude of precipitation, the seasonal evolution of rainfall is very well represented by the simulations, as the onset and retreat dates are in close agreement with the observations.

Finally, the simulated rainfall in the Amazon is in very good agreement with the observations during austral winter (Figure

280   9d). The models also show a good representation of the transition from winter to summertime rainfall by representing with relative skill the smooth transition from 4 mm day^{-1} in September to 6 mm day^{-1} in November and close to 8 mm day^{-1} in late December. However, peak summertime rainfall in January and February is underestimated by all the simulations. The low resolution simulations, after simulating an annual maximum of rainfall in December, simulate a decrease in precipitation for January and February, whereas the observations show the opposite behaviour. Rainfall in the Amazon from January to March,

285   in both TRMM and CHIRPS, is close to 10 mm day^{-1}, yet the low resolution simulations present rainfall rates of 8 mm day^{-1} or even less in mid-February. GC3.1 N216 shows a better agreement with observations but still underestimates summertime rainfall by 1 mm day^{-1}, outside of the uncertainty range of TRMM.

4.3   OLR and q

The seasonal cycles of out-going longwave radiation (OLR), vertical velocity (ω) and specific humidity (q) are key features of

290   a monsoon since these quantities characterise the strength and height of deep convection and the mid-level moisture. Figure 10 shows the pentad-mean annual cycle of OLR, q and ω at the 500-hPa level in four regions of the AMS, as in section 4.2. For the North American Monsoon the seasonal cycle of OLR, q and ω is relatively well represented in the simulations. During late boreal winter and early spring, OLR increases steadily as a result of surface warming. However, in early June, close to monsoon onset (Douglas et al., 1993; Geil et al., 2013), OLR sharply decreases reaching a minimum value of 246 W m^{-2}

295   by mid-July. The vertical velocity decreases steadily from January to a minimum in August, indicating ascent from May 1st until September 15th. The models show similar seasonal cycles but overestimate the summertime OLR by $\approx$ 6 W m^{-2} and underestimate mid-level moisture by 0.3 g/kg and ω by 0.01 Pa s^{-1}. After convective activity decreases in late August in ERA-5, OLR increases to a local maxima of $\sim$ 271 W m^{-2} on mid-September, q decreases significantly and ω turns positive. The simulated shallower convection and drier mid-troposphere may be compensated by stronger ascent in the mid-troposphere.

300   In the MSD region, OLR and q show signs of convective activity from mid-April, as OLR decreases and moisture increases steadily from April until June. The characteristic MSD bimodal distribution can also be observed as two peaks of low OLR,

high q and low ω indicative of strong ascent. These periods are separated by a period of higher OLR, lower q and weaker ascent found from June 15 until late August. ERA5 data show that during the midsummer drought period OLR increases by 10 W m^{-2}, ω decreases by 0.015 Pa s^{-1} and q decreases by 0.5 g/kg. Arguably with a small dry bias with shallower convection after

305 mid-July, the simulations follow closely the observed seasonal cycle. The simulated first peak of rainfall has similar OLR and mid-level moisture but stronger ascending motions, which may explain the positive rainfall bias in this period showed in Figure 9a. Moreover, between the first peak and the midsummer drier period, the simulated OLR increases from 220 W m^{-2} in June 15 to 250 W m^{-2} by Aug 1. In the same period, the simulated moisture and ascent decrease more sharply than observations. This stronger than observed changes to the characteristics of convection are consistent with the sharper than observed midsummer

310 drought in the simulations showed in Figure 9a. The second peak of rainfall is also simulated to be weaker in terms of mid-level moisture and height of convection when compared to ERA5 but of similar magnitude in terms of ω. The characteristics of the retreat stage of rainfall at the start of October shows close agreement between reanalysis and simulations.

In southeastern Brazil, the strong seasonal differences characterised by a (wet) season of low OLR, strong ascent and high q from November to February and another (dry) season with high OLR and low q and positive ω from April to October. The

315 simulations reasonably follow the annual cycle of these metrics, particularly during austral winter. For example, the observed q in the dry seasons of austral fall, winter and spring in ERA5 is very similar to the simulated q in these seasons. However, during austral summer when monsoon rainfall is prominent, the simulations show significant biases characterised by stronger ascent and higher levels of mid-level moisture, although the height of convection (OLR 225 W m^{-2}) is only modestly higher in the simulations.

320 The seasonal cycle of convective activity in the Amazon basin is similar to that of southeastern Brazil but with a longer wet season and a wetter dry season, as shown by Figure 9. The simulated OLR, q and ω exhibit the highest biases in the Amazon. During austral summer, particularly January and February, the simulated convective activity is shallower (OLR bias of +25 W m^{-2}) and weaker (positive ω bias +0.02 Pa s^{-1}) and the mid-level troposphere is drier (-0.5 g/kg) than in ERA5. In spite of biases in the magnitude of OLR, q and ω during peak convective activity, the seasonal variation is very well simulated so

325 that convective activity, as evidenced by these metrics, starts and ends in the simulations within one or two pentads of the reanalysis. The smallest biases are found for the GC3 N216-pi simulation, whereas the rest of the simulations exhibit very similar characteristics in this and the other three regions.

5 ENSO Teleconnections

El Niño-Southern Oscillation (ENSO) teleconnections are the prominent source of interannual variability in the AMS. This

330 section documents the temperature, sea-level pressure (SLP) and precipitation responses in the AMS to observed and simulated El Niño and La Niña events. ENSO events were defined in simulations and observations as those months where the El Niño 3.4 index was above or below 0.65 (Trenberth, 1997). Other indices, including the use of a 5-month running mean (Trenberth et al., 1998) and other threshold values were tested, without significantly changing the results.

The near-surface air temperature and SLP response to El Niño and La Niña events is shown in Figure 11 for model and
335   ERA5. The modelled warm anomaly during El Niño events in the East Pacific Ocean does not extend to the east as much as
the observed warm anomaly. However, the simulated and observed teleconnection pattern to South-America, i.e, regions of
positive temperature anomalies are very similar. The cold anomalies during La Niña events in northern South America are
seemingly well simulated as well. However, the cold anomalies during La Niña events in the equatorial Central Pacific are, on
average, colder in the simulations. The teleconnection to southern North America, i.e., colder (warmer) conditions during El
340   Niño (La Niña) events are relatively well simulated even though the low resolution simulations showed a broader and stronger
than observed response in southeastern US. The simulated teleconnection pattern to North America is better represented in
GC3 N216-pi which can be observed as a modest cooling (warming) in northern Mexico and soutwestern US during El Niño
(La Niña) events.

The SLP response to ENSO events is mostly observed in the subtropical high pressure systems (Vera et al., 2006; Marengo
345   et al., 2012). In particular, the response in the northern Pacific and Atlantic, known as the Pacific North-American pattern
provide insight into the Rossby wave source and the effect on the midlatitude jet arising from ENSO events. A weakened North
Pacific Subtropical High is observed in ERA5, with an SLP anomaly of -4 hPa off the coast of California. The models show
a similar but smaller SLP response in the same region. In the North Atlantic, positive ENSO events produce a negative NAO
response, with opposite response for negative ENSO events. While the models seem to be able to capture this response of
350   Atlantic SLP, the simulated response is weaker in the low resolution simulations.

The rainfall anomalies to ENSO events are shown in Figure 12. Three regions in the AMS have a significant precipitation
response to ENSO events in the observations and simulations. In southern North America, rainfall increases (decreases) during
El Niño (La Niña) events due to the effect of Rossby waves on the subtropical jet and wintertime midlatitude disturbances
(Vera et al., 2006; Bayr et al., 2019). The GPCP dataset (Figure 12a, b) shows significant boreal winter rainfall increases in
355   southeastern US and the Gulf of Mexico during El Niño events, and an opposite response to La Niña phases. All the simulations
sensibly reproduce this teleconnection rainfall pattern.

The core Amazon basin shows the strongest response to ENSO events in the observations. This teleconnection works through
the perturbation of ENSO to the Walker circulation (Vera et al., 2006; Cai et al., 2019). Strong positive (negative) rainfall
anomalies during the negative (positive) phases of ENSO in northern South America are observed in GPCP. All the simu-
360   lations show a very similar and statistically significant response. The strongest simulated response is that of GC3 N96-pi,
especially over eastern Brazil and the equatorial Atlantic Ocean. The models also show the observed response in the third
region, southeastern south America, which shows an opposite sign response to ENSO events to that of the Amazon (Vera et al.,
2006).

Figure 13 shows the observed and simulated precipitation responses in four regions of the AMS to different magnitudes of
365   ENSO events. The degree of linearity of ENSO teleconnections to the AMS may suggest how the perturbation in precipitation
to ENSO events scales with the magnitude of the event. While the observed response shows some degree of linearity for El Niño
events in South America (panels c, d), the majority of the observed responses, particularly to La Niña phases, are not linear.
However, the simulations show several signs of linearity; for instance the historical experiments exhibited a linear response in

precipitation to ENSO events in North America and southeastern South America. However, some simulated responses, e.g. to

370 La Niña phases in South America in the piControl simulations, show signs of non-linearity.

6 Summary and discussion

This study analysed and compared the simulated climate in the AMS in piControl and historical experiments of two CMIP6 models: UKESM1 and HadGEM3.0. A schematic in Figure 14 shows the primary components of the AMS climate and main biases in these simulations. The temperature biases, shown in Figures 1 and 3, showed significant differences of up to 4

375 K between simulated and observed climate. For example, the warm positive bias over the Amazon during austral summer. This warm bias is likely linked to cloud cover during peak activity of the South American Monsoon. The land-sea temperature contrast is likely affected by this significant bias in Amazonian temperature, thereby playing a role in the also biased circulation in southeastern South America. The historical experiments showed an average warming of 2 K as a response to historical forcing in most of the regions, as shown when compared to their corresponding piControl simluations in Figure 3. This warming

380 led to warmer than observed tropical SSTs in all seasons and a particularly strong warming signal in summer in southwestern North America. These temperature differences suggest that UKESM1 has a higher sensitivity to historical forcing in the AMS region, as found by Andrews et al. (2019).

The simulations showed a biased Atlantic ITCZ that was displaced south of observations, particularly during boreal winter and in the low resolution simulations. The bias in the ITCZ are likely intertwined with biases in ascending and descending

385 motions in the East Pacific and Atlantic Oceans, which were shown to be characterised, in the Atlantic region, by positive vertical velocity biases south of the equator. The biased ITCZ position in the Atlantic and the biases in the Walker circulation are likely intertwined with the South American Monsoon region, where simulated rainfall was displaced to the southeast.

The pentad-mean annual cycle of precipitation was analysed for four key regions of the AMS. Figure 9 showed that the simulations represented reasonably well the seasonal variations and timings of monsoon precipitation, particularly in the regions

390 of the Midsummer Drought and the North American Monsoon. Similarly, the Midsummer Drought bimodal regime in southern Mexico and Central America, a feature that most models have difficulty capturing (Ryu and Hayhoe, 2014), is relatively well represented. The seasonal cycle of rainfall is characterised in both simulated and observed datasets as two rainfall maxima separated by a drier period. In other words, the bimodal regime shows stronger a intraseasonal variation in these models. The first peak and dry periods were found to have lower mean rainfall rates in the historical experiments. The characteristics of this

395 regime (e.g. the strength of the first peak in rainfall) varied amongst the different experiments, suggesting a modelled sensitivity to SSTs.

The biased wetter than observed southeastern Brazil and drier than observed Amazon are a consistent characteristic of all the simulations. During the period of maximum mean rainfall rates in February, the simulations can overestimate rainfall by 3 mm day^{-1} in southeastern Brazil and underestimate rainfall in the Amazon by a similar rate. The historical experiments showed

400 a small drying response to historical forcing in the Amazon therefore slightly increasing the magnitude of this dry bias. The simulated Amazon river basin also had shallower convection (higher OLR), less precipitation and higher temperature than in

the observations, whereas the opposite is true for southeastern Brazil, Bolivia and Paraguay. The biased Atlantic ITCZ and austral summer low-level circulation are likely responsible for the biased distribution of precipitation in the South American Monsoon.

405   The simulated rainfall anomalies during the positive phase of ENSO in North America and South Eastern South America are in close agreement with observations in both spatial pattern and magnitude. Similarly, and inspite of rainfall biases in the region discussed above, the teleconnection bewtween ENSO and Amazonian rainfall is also well represented in spatial distribution for both phases of ENSO. ENSO teleconnections in these simulations were found to be linear, i.e., the precipitation response is linearly related to the magnitude of the SST perturbation in the central Pacific. In this model framework, positive and negative

410   phases produce the opposite and equivalent precipitation response in the AMS. However, observations show scarce signs of linearity, which may come from the significant difference in sample sizes or missing processes or sources of variability, such as other tropical teleconnection mechanisms.

    Most of the common biases in both piControl and historical experiments are significantly reduced in the higher resolution simulation. In contrast, the biases in the piControl simulation from the Earth System Model, UKESM1, are essentially the same

415   to those of the ocean-atmosphere coupled model GC3-N96-pi. However, the historical experiments did show a significantly different response to forcing in circulation, temperature and precipitation. In short, the main dynamical biases, such as the biased austral summer circulation in South America, are only improved when the resolution is increased, whereas the addition of Earth System processes only has an influence on the response to forcing but does not improve dynamical biases in the AMS significantly.

420   The biases diagnosed in the tropical Atlantic and Pacific Oceans suggest that the improvement of SST biases, and related ITCZ and Walker circulation biases will significantly improve the representation of rainfall in the South American Monsoon for these models. The seasonal cycle and spatial distribution of rainfall in some regions of the AMS, such as the North American Monsoon, is very well simulated, encouraging further analysis of these models to understand future projections, climate variability or teleconnections.

425   *Author contributions.* JLGF conducted the analyses, LJG and SO directed the research. All authors were fully involved in the revisions and the preparation of the paper.

Competing interests. The authors declare that there are no competing interests.

Data availability. ERA5 data was made available by Copernicus at https://cds.climate.copernicus.eu whereas the model data is available in the CMIP6 Earth System Grid Federation (ESGF) at https://esgf-index1.ceda.ac.uk/projects/cmip6-ceda/.

430   *Acknowledgements.* JLGF was funded by an Oxford-Richards Scholarship.

Weather and Climate Dynamics Discussions — Open Access — EGU
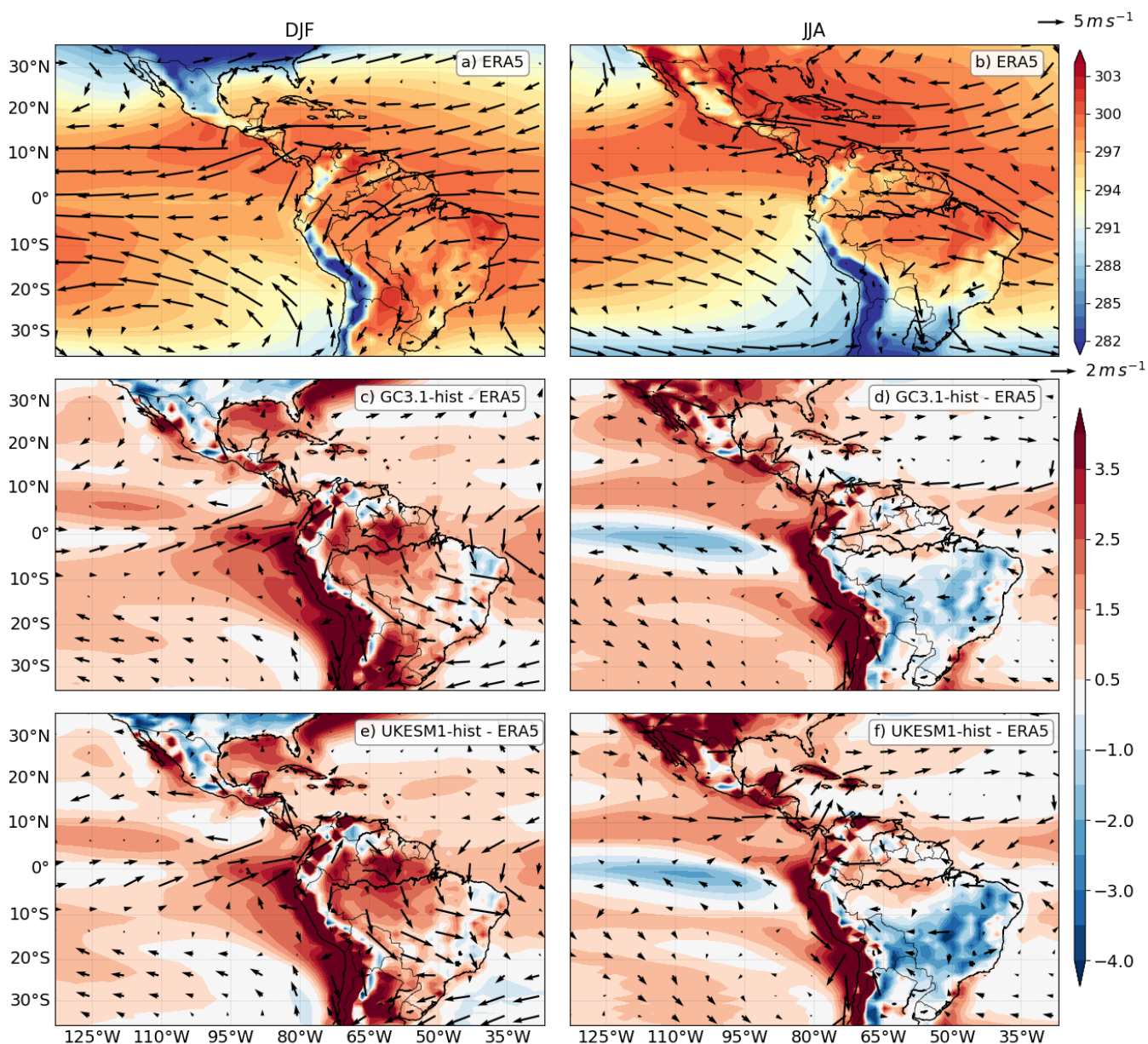
Figure 1. (a, b) Temperature (color-contours in K) and wind speed (vectors) at 850 hPa DJF and JJA climatogies in ERA5. The biases are shown as the differences between the ensemble mean from the historical experiment of (c, d) GC3 and (e, f) UKESM1 and ERA5. The climatogies and biases are shown for (a, c, e) boreal winter (DJF) and (b, d, f) boreal summer (JJA). Only differences statistically significant to the 95% level are shown, according to a Welch t-test for each field. The key for the size of the wind vectors is shown in the top right corner of panels b) and d).
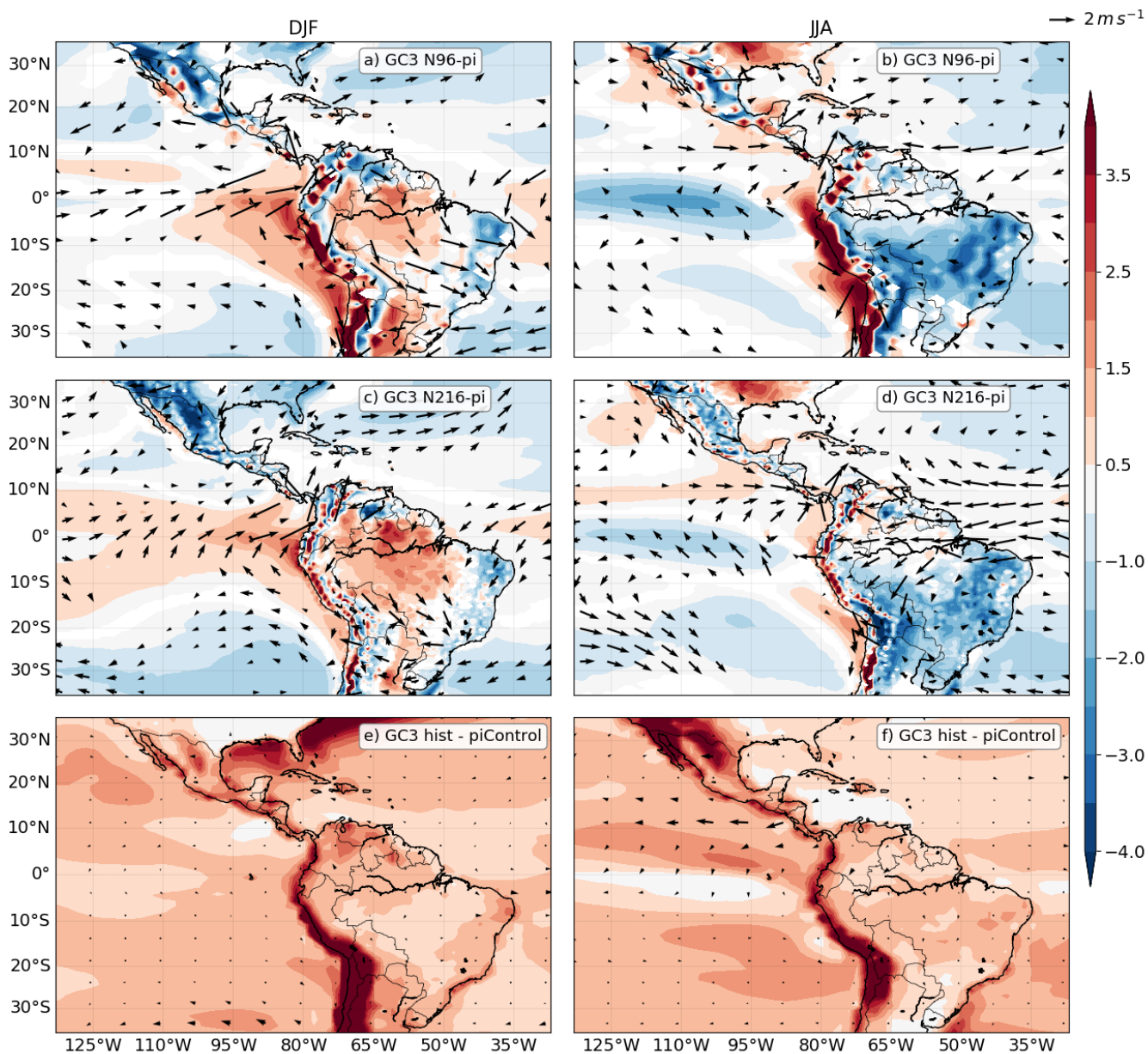
Figure 2. As in Figure 1, but showing the differences between the piControl simulations of (a, b) GC3 N96-pi and (c, d) GC3 N216-pi, and ERA5. (e, f) show the difference between the historical (1979-2014) and piControl experiments of GC3.
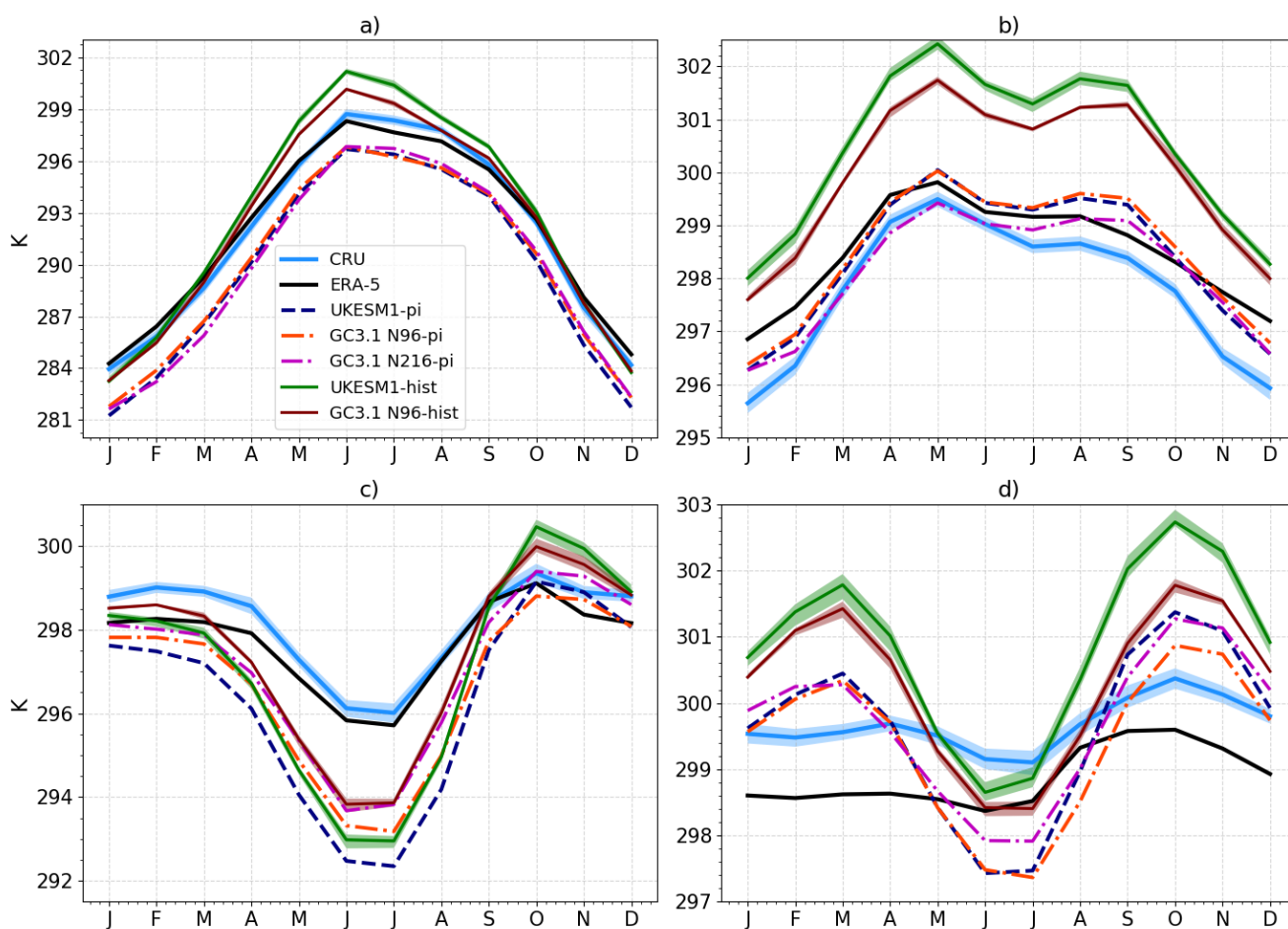
Figure 3. Monthly-mean temperature in the (a) North American Monsoon [19-35°N,110-103°W], (b) the Midsummer drought [11-19°N,95-85°W] (c) Eastern Brazil [20-10°S,60-40°W] and (d) the Amazon basin [-10-0°S,75-50°W] regions. The shadings for the CRU dataset represents the observational uncertainties and for the historical simulations the shading is the ensemble spread.
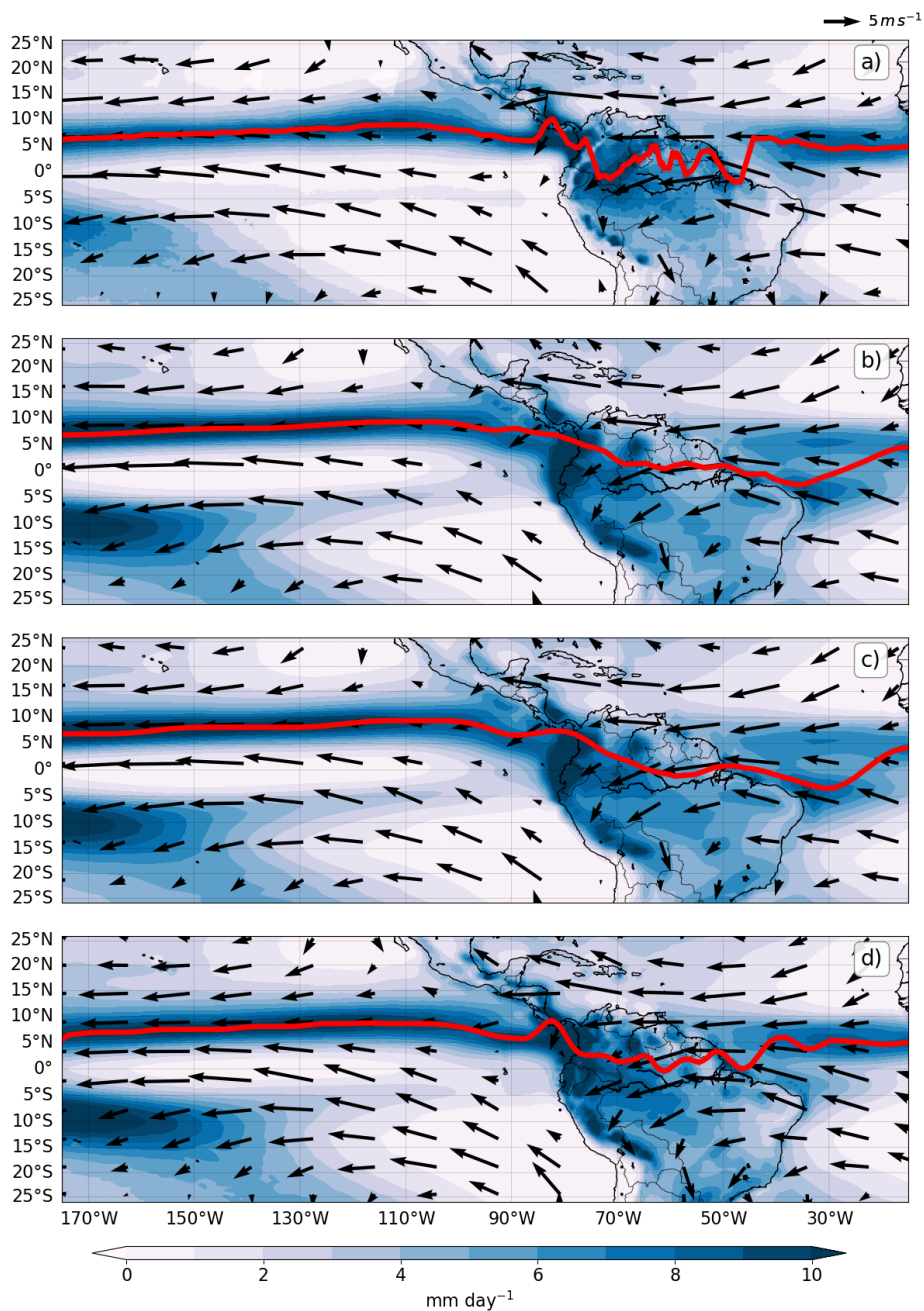
Figure 4. Climatological rainfall and low-level wind speed (850-hPa) in (a) TRMM and ERA-5, (b) the ensemble-mean UKESM-historical, (c) GC3 N96-pi and (d) GC3 N216-pi. The red line highlights the maximum rainfall for each longitude as a proxy for the position of the ITCZ.
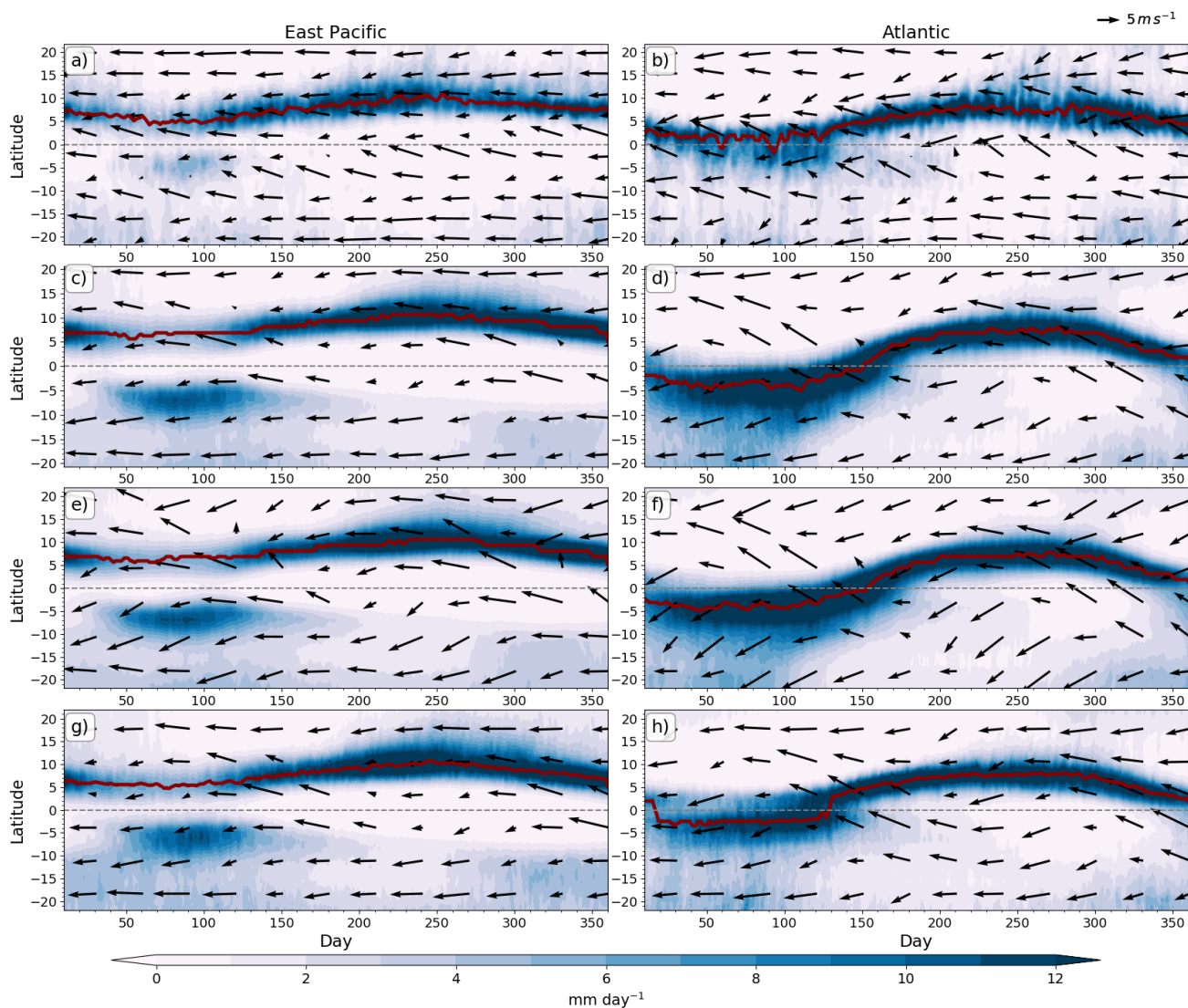
Figure 5. Time-Latitude section of daily mean rainfall (colour contours) and low-level wind speed (850 hPa) longitudinally averaged over the (a, c, e, g) East Pacific [150°W-100°W] and (b, d, f, h) Atlantic [40°W-20°W] Oceans. (a, b) show rainfall from TRMM and winds from ERA-5, (c, d) the ensemble-mean UKESM-historical, (e, f) GC3 N96-pi and (g, h) GC3 N216-pi. The red solid line shows the ITCZ as the latitude of maximum precipitation.
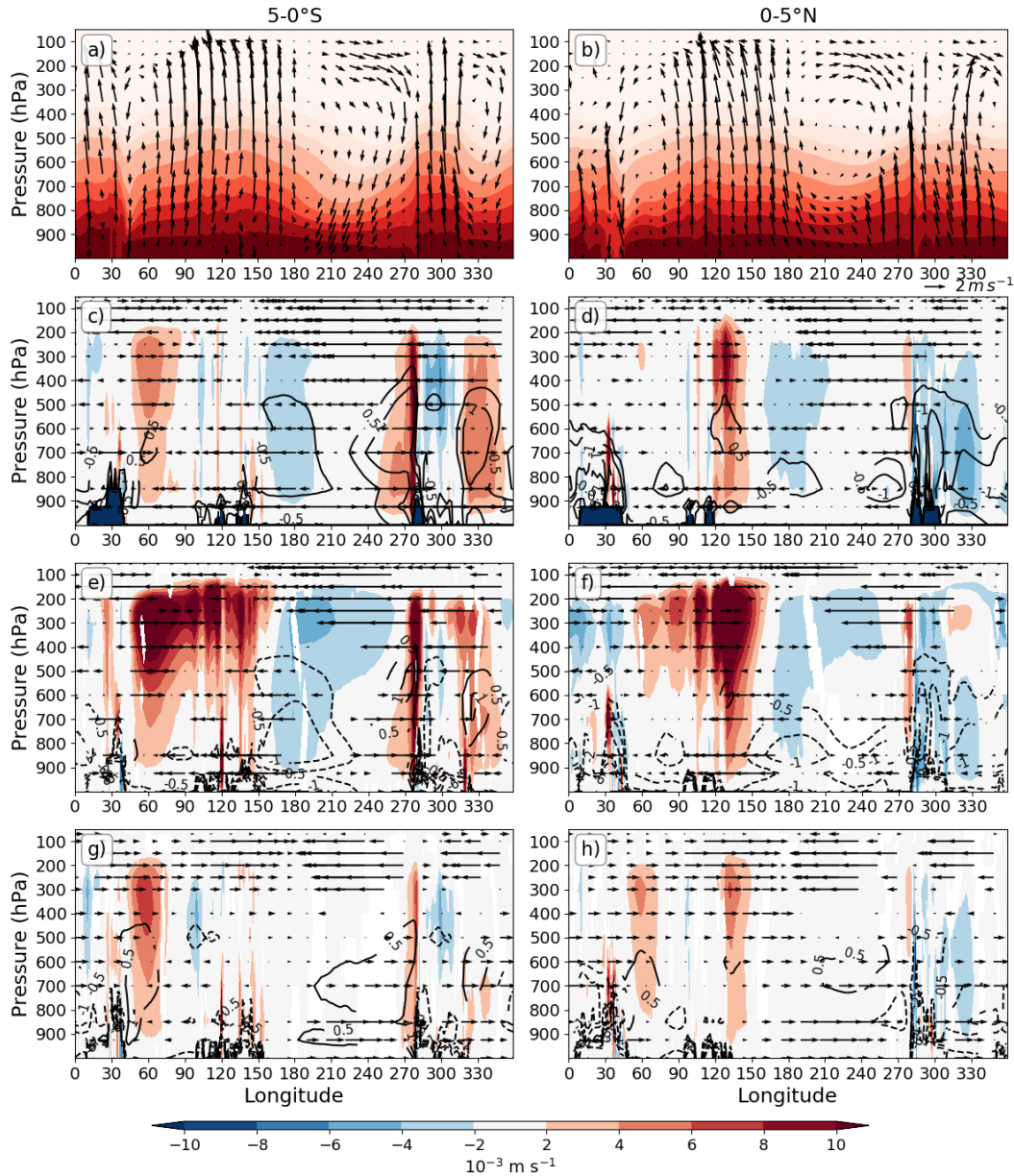
Figure 6. Longitude-pressure level plots of the mean DJF (a, b) specific humidity (color contours) and zonal and vertical velocities (vectors) in ERA5. (a) is latitudinally averaged in 5-0°S and (b) in 0-5°N. (c, d, e, f, g, h) show the bias in vertical velocity (color-contours), zonal wind (vectors) and specific humidity (line contours). Biases are shown for (c, d) UKESM1-historical, (e, f) GC3.1 N96-pi and (g, h) GC3.1 N216-pi. Only biases statistically significant to the 95% confidence level are shown, according to a Welch t-test between model and ERA5 data for all fields.
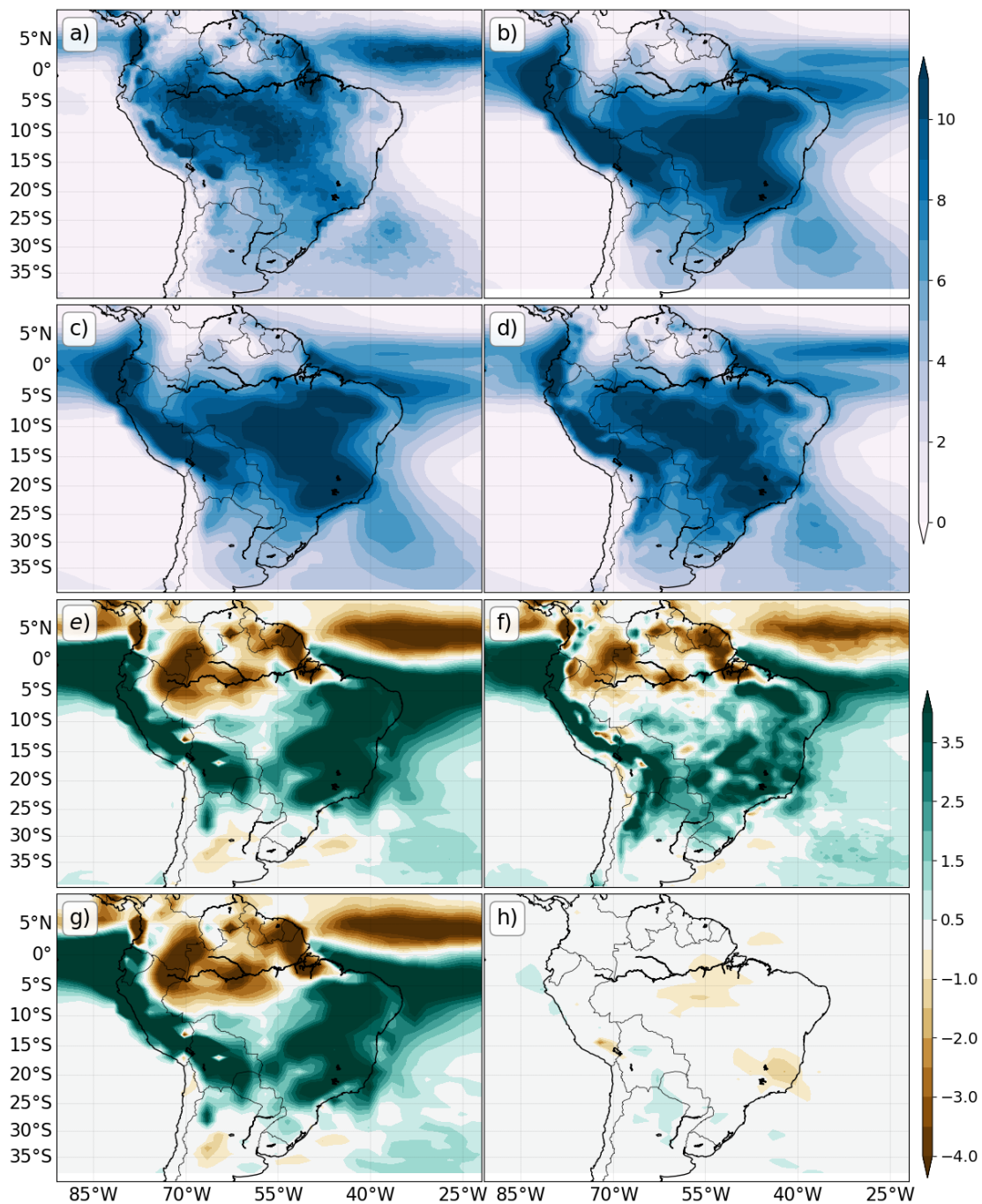
Figure 7. DJF mean rainfall in (a) TRMM, (b) UKESM1-historic, (c) GC3.1 n96 and (d) GC3.1 n216 DJF in mm day^{-1}. (e, f, g) show the statistically significant differences between panels (c, d, e) and (a) TRMM, respectively. (f) shows the difference between UKESM-historical and UKESM1-pi.
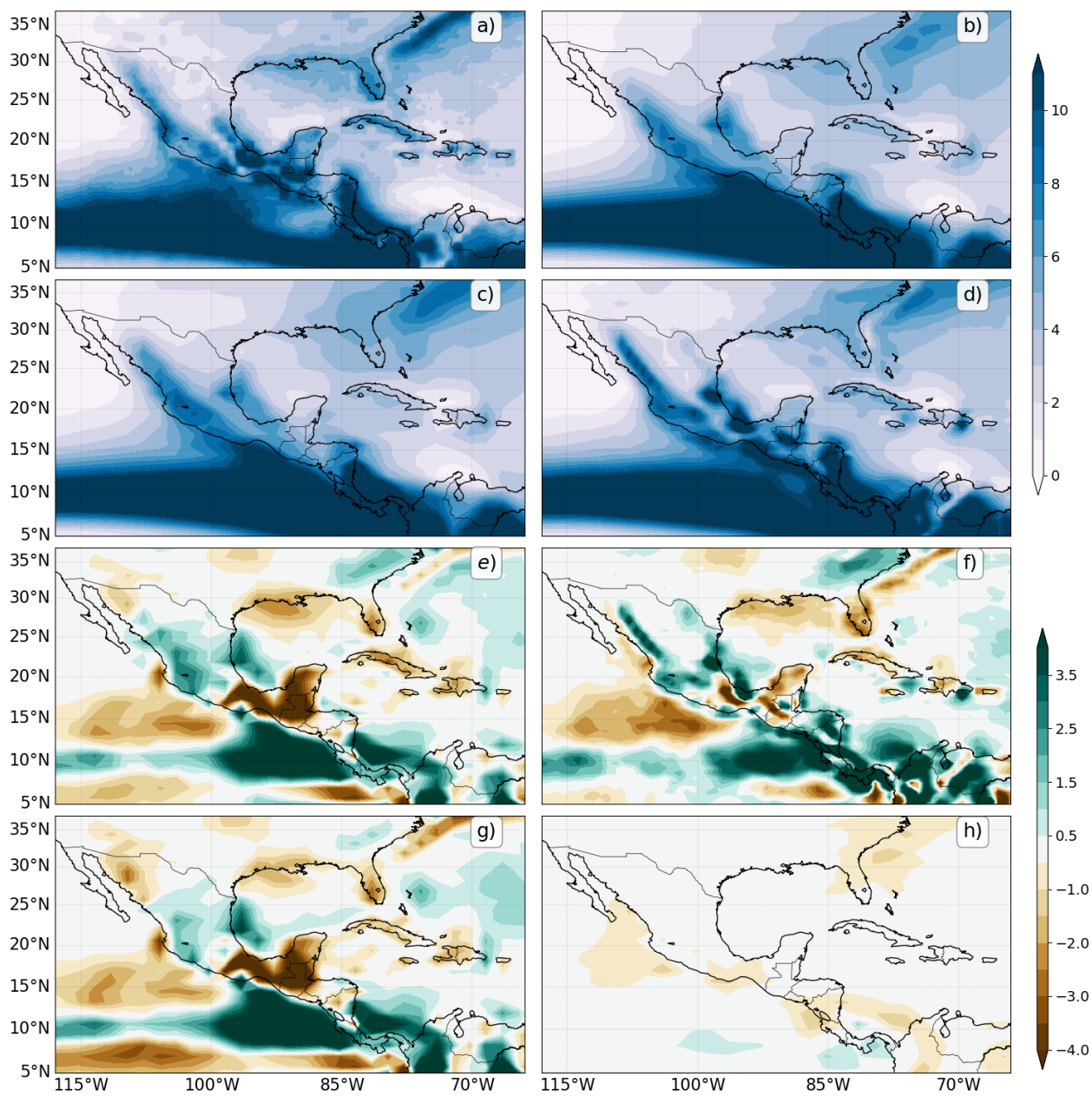
Figure 8. As in Figure 7 but for JJA in the northern part of subtropical America.
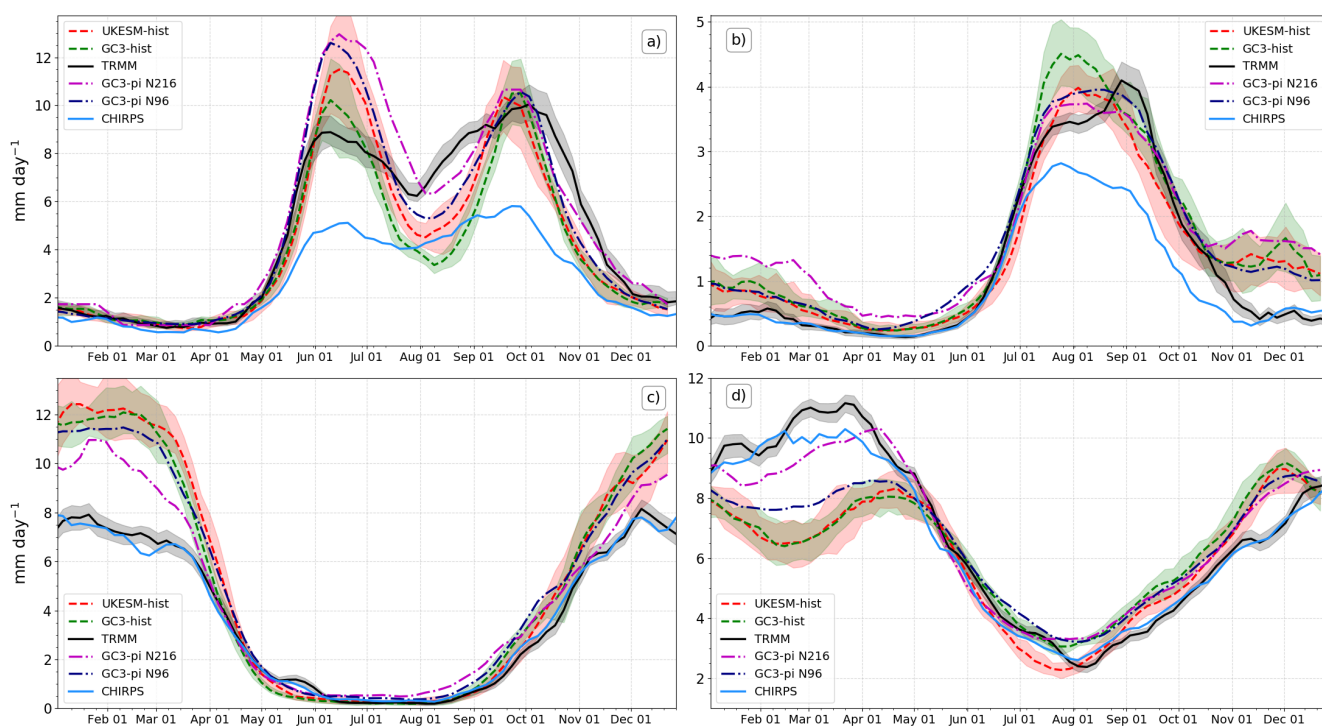
Figure 9. Annual cycle of pentad-mean rainfall in the regions (a) the Midsummer drought, (b) the North American Monsoon, (c) Eastern Brazil and (d) the Amazon Basin. The regions are defined as in Figure 3. The shaded regions represent observational uncertainty for TRMM and ensemble spread for the historical experiments.
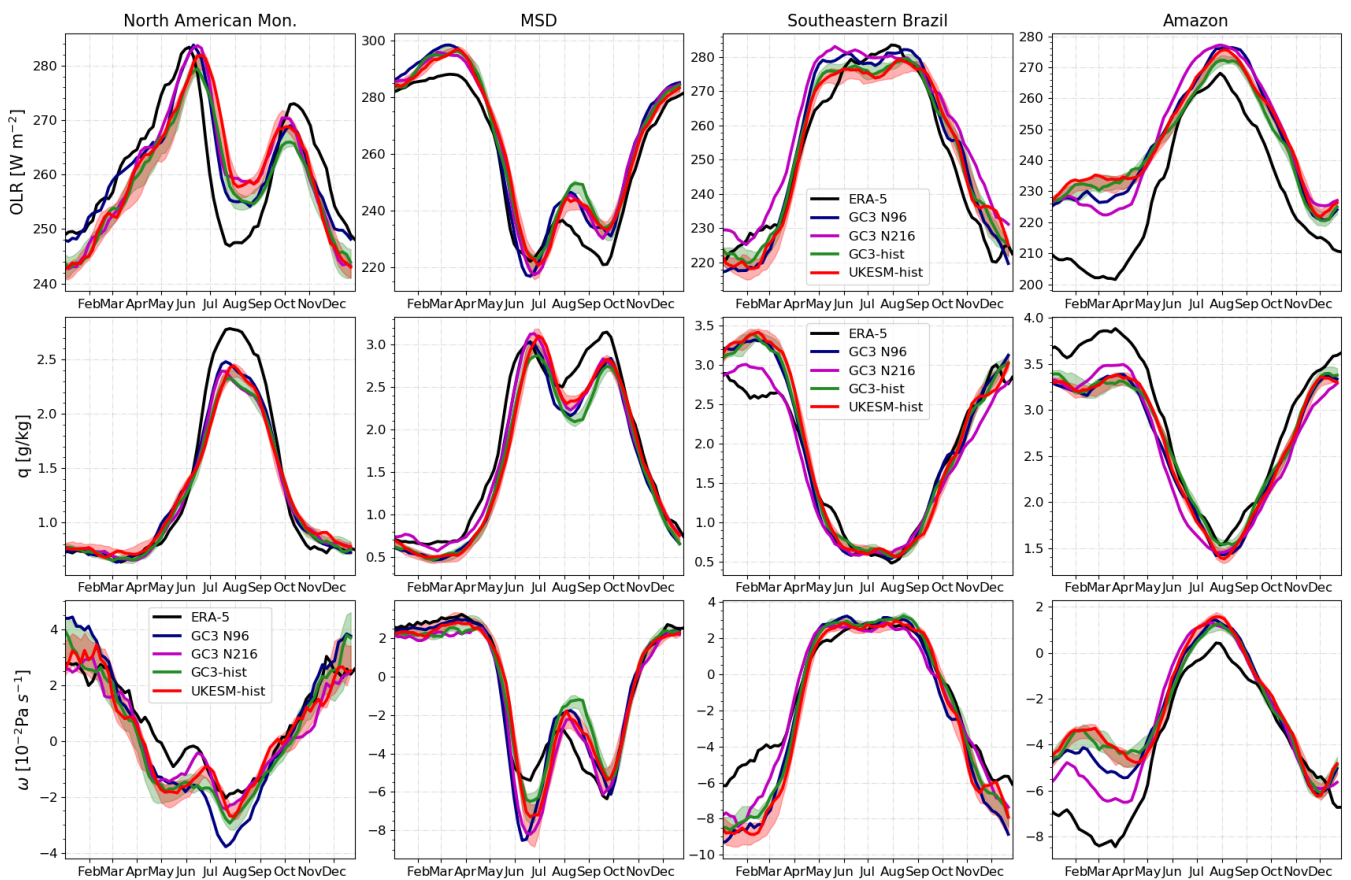
Figure 10. Pentad-mean (upper) out-going longwave radiation (OLR), (middle) specific humidity at 500-hPa and (lower) ω 500-hPa. These are shown from left to right for the North American Monsoon, the Midsummer drought, southastern Brazil and the core Amazon.
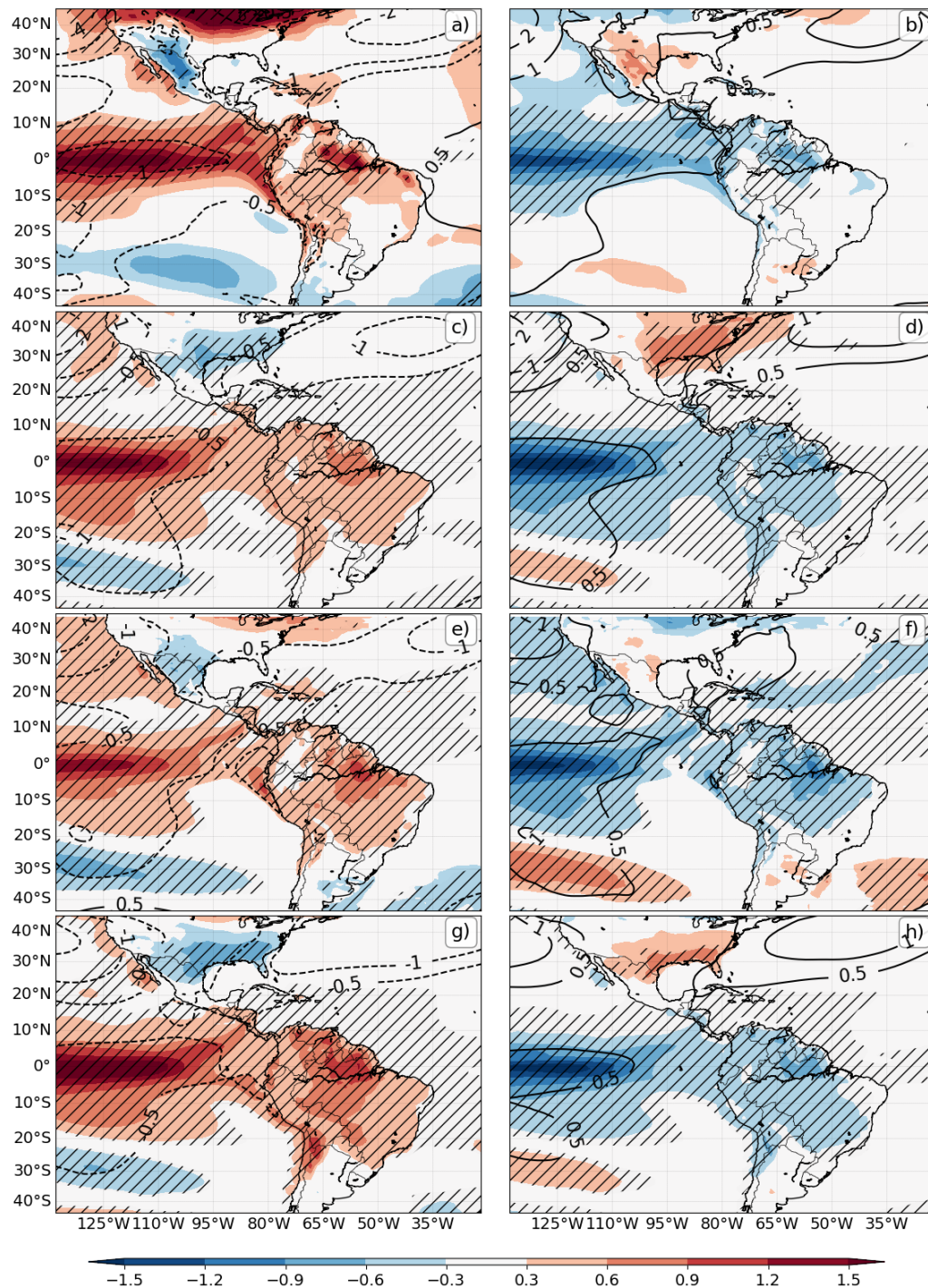
Figure 11. DJF Temperature anomalies (colour contours in K) and SLP (line contours in hPa) during (a, c, e, g) El Niño and (b, d, f, h) La Niña events. Results are shown for (a, b) ERA-5, (c, d) UKESM1-historical, (e, f) GC3 N96-pi and (g, h) GC3 N216-pi. The hatched regions denote 99% significance from a Welch t-test for the temperature field.
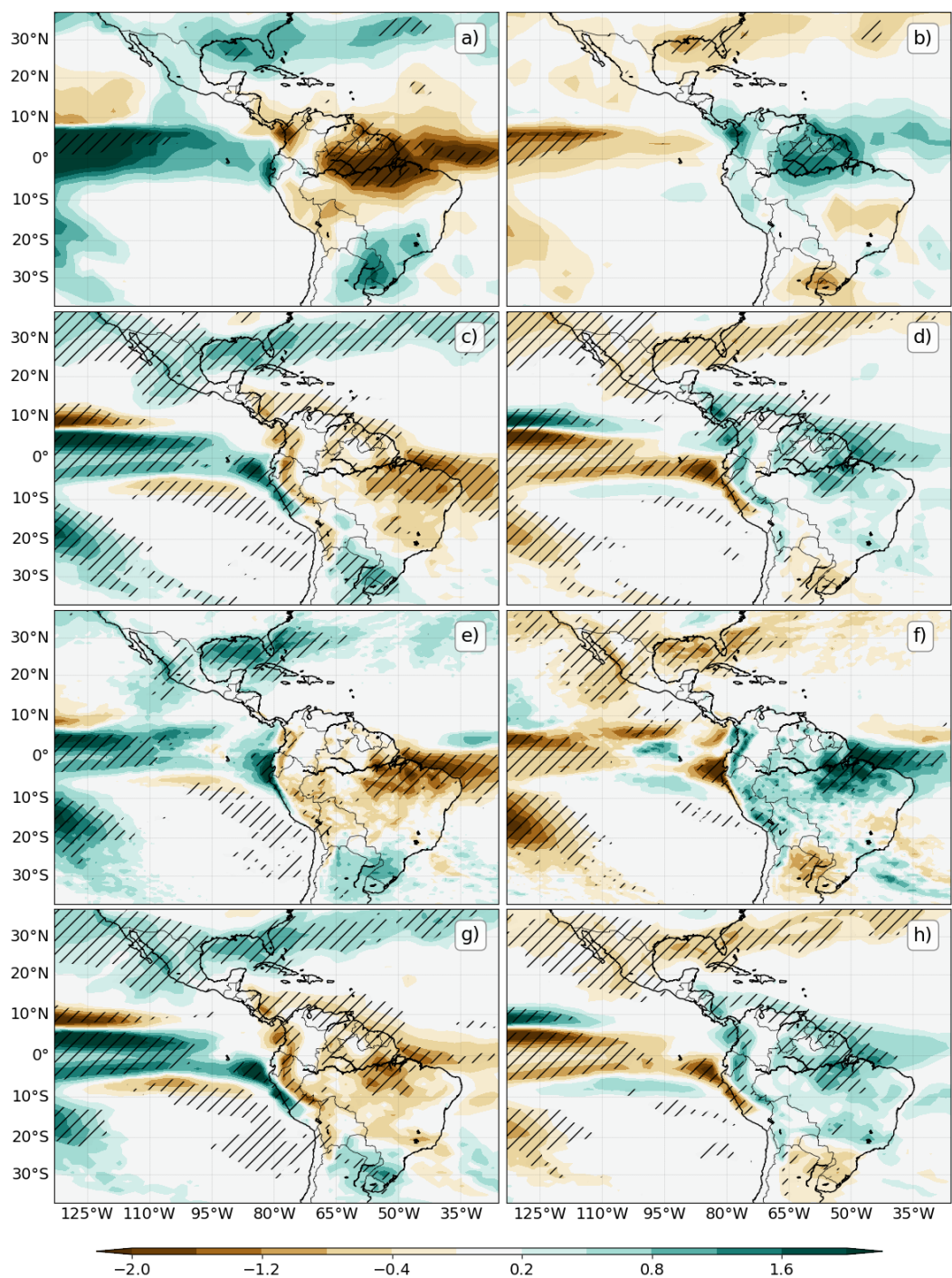
Figure 12. As in Figure 11 but for the rainfall response [mm day^{-1}] using GPCP as the observational dataset.
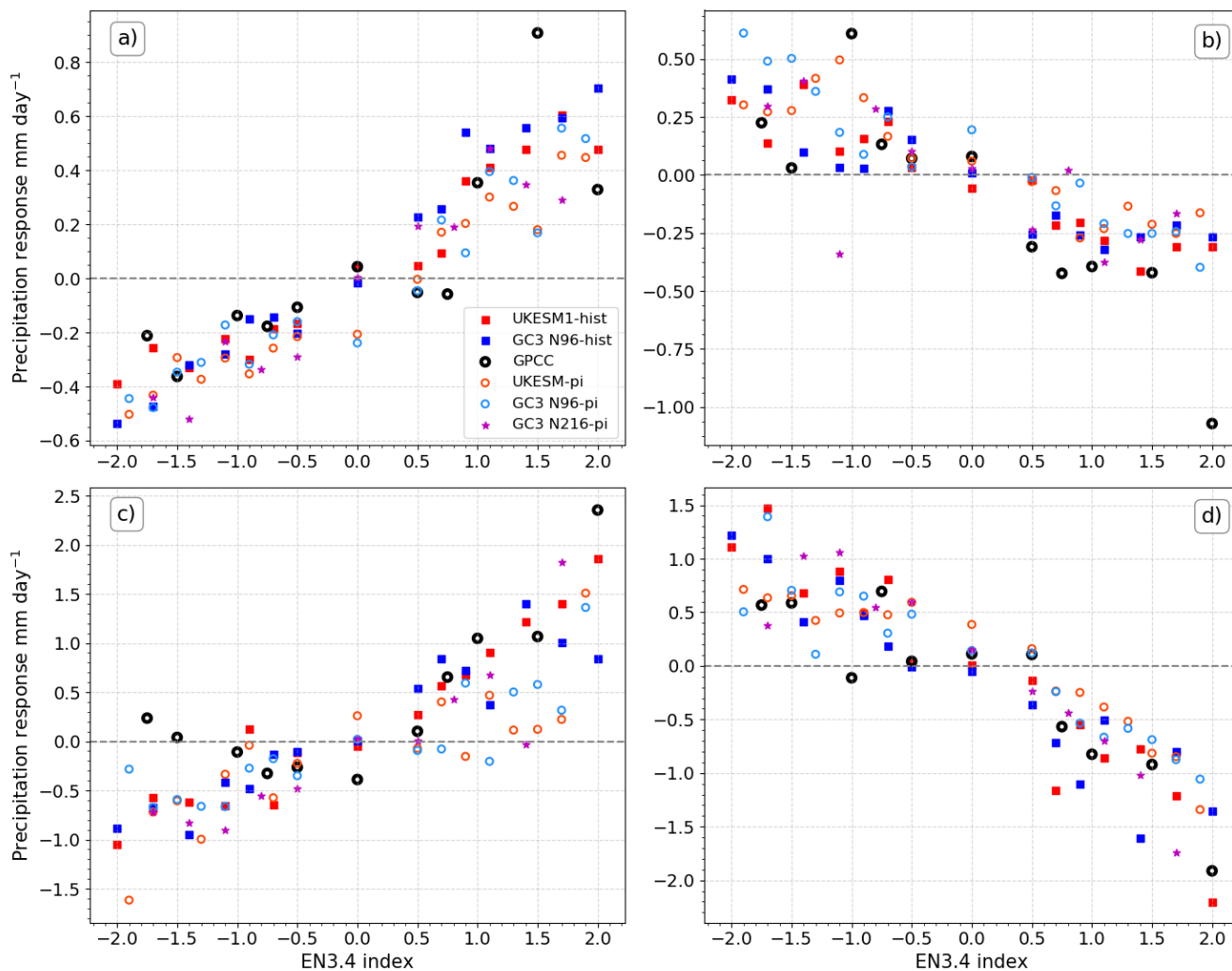
Figure 13. Precipitation response [mm day^{-1}] as a function of the El Niño 3.4 index (see text) for (a) southwestern North America [20-37°N, 112-98°W], (b) Central America and southern Mexico [5-19°N, 95-83°W],, (c) South Eastern South America [35-25°S, 60-50°W], and (d) the Amazon [10-0°S, 70-45°W]. The observation scatter points are from GPCC in the period of 1940-2013.
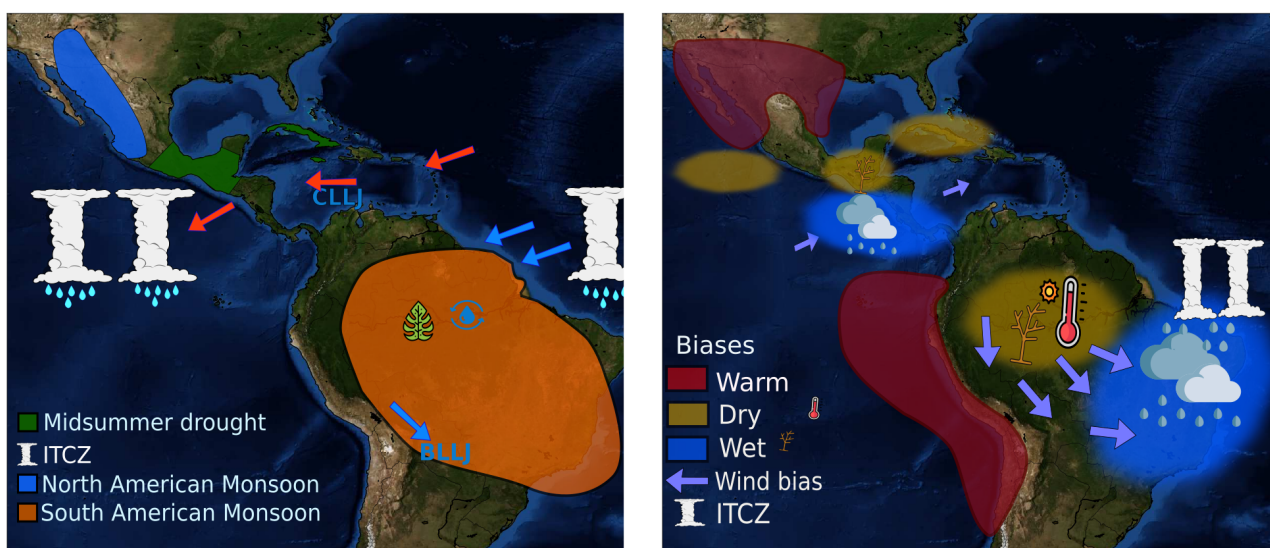
Figure 14. Schematics of (left) the main features in the AMS and (right) the main biases in UKESM1 and HadGEM3. In (a) the boreal summer easterlies (red) and austral summer circulation (blue) are shown with the Caribbean and Bolivian Low-level Jets (CLLJ and BLLJ, respectively). In (b) the biases are shown for the respective northern and southern Hemisphere summers. The ITCZ bias in (b) refers to the southward displacement bias of the Atlantic ITCZ in the simulations.

References

Adams, D. K. and Comrie, A. C.: The north American monsoon, Bulletin of the American Meteorological Society, 78, 2197–2214, 1997.

Adler, R. F., Huffman, G. J., Chang, A., Ferraro, R., Xie, P.-P., Janowiak, J., Rudolf, B., Schneider, U., Curtis, S., Bolvin, D., Gruber, A., Susskind, J., Arkin, P., and Nelkin, E.: The version-2 global precipitation climatology project (GPCP) monthly precipitation analysis (1979–present), Journal of hydrometeorology, 4, 1147–1167, 2003.

Andrews, T., Andrews, M. B., Bodas-Salcedo, A., Jones, G. S., Kuhlbrodt, T., Manners, J., Menary, M. B., Ridley, J., Ringer, M. A., Sellar, A. A., et al.: Forcings, feedbacks, and climate sensitivity in HadGEM3-GC3. 1 and UKESM1, Journal of Advances in Modeling Earth Systems, 11, 4377–4394, 2019.

Arritt, R. W., Goering, D. C., and Anderson, C. J.: The North American monsoon system in the Hadley Centre coupled ocean-atmosphere GCM, Geophysical Research Letters, 27, 565–568, 2000.

Bayr, T., Domeisen, D. I., and Wengel, C.: The effect of the equatorial Pacific cold SST bias on simulated ENSO teleconnections to the North Pacific and California, Climate Dynamics, pp. 1–19, 2019.

Becker, A., Finger, P., Meyer-Christoffer, A., Rudolf, B., and Ziese, M.: GPCC full data reanalysis version 6.0 at 1.0: monthly land-surface precipitation from rain-gauges built on GTS-based and historic data, Global Precipitation Climatology Centre (GPCC): Berlin, Germany, 2011.

Bombardi, R. J. and Carvalho, L. M.: The South Atlantic dipole and variations in the characteristics of the South American Monsoon in the WCRP-CMIP3 multi-model simulations, Climate Dynamics, 36, 2091–2102, 2011.

C3S: ERA5: Fifth generation of ECMWF atmospheric reanalyses of the global climate., Copernicus Climate Change Service Climate Data Store (CDS), date of access: 18 March 2019, https://climate.copernicus.eu/climate-reanalysis, 2017.

Cai, W., Wu, L., Lengaigne, M., Li, T., McGregor, S., Kug, J.-S., Yu, J.-Y., Stuecker, M. F., Santoso, A., Li, X., Ham, Y.-G., Chikamoto, Y., Ng, B., McPhaden, M. J., Du, Y., Dommenget, D., Jia, F., Kajtar, J. B., Keenlyside, N., Lin, X., Luo, J.-J., Martín-Rey, M., Ruprich-Robert, Y., Wang, G., Xie, S.-P., Yang, Y., Kang, S. M., Choi, J.-Y., Gan, B., Kim, G.-I., Kim, C.-E., Kim, S., Kim, J.-H., and Chang, P.: Pantropical climate interactions, Science, 363, eaav4236, 2019.

Carvalho, L. M., Jones, C., and Liebmann, B.: The South Atlantic convergence zone: Intensity, form, persistence, and relationships with intraseasonal to interannual activity and extreme rainfall, Journal of Climate, 17, 88–108, 2004.

Colorado-Ruiz, G., Cavazos, T., Salinas, J. A., De Grau, P., and Ayala, R.: Climate change projections from Coupled Model Intercomparison Project phase 5 multi-model weighted ensembles for Mexico, the North American monsoon, and the mid-summer drought region, International Journal of Climatology, 38, 5699–5716, 2018.

Douglas, M. W., Maddox, R. A., Howard, K., and Reyes, S.: The mexican monsoon, Journal of Climate, 6, 1665–1677, 1993.

Eyring, V., Bony, S., Meehl, G. A., Senior, C. A., Stevens, B., Stouffer, R. J., and Taylor, K. E.: Overview of the Coupled Model Intercomparison Project Phase 6 (CMIP6) experimental design and organization, Geoscientific Model Development (Online), 9, 2016.

Funk, C., Peterson, P., Landsfeld, M., Pedreros, D., Verdin, J., Shukla, S., Husak, G., Rowland, J., Harrison, L., Hoell, A., and Michaelsen, J.: The climate hazards infrared precipitation with stations—a new environmental record for monitoring extremes, Scientific data, 2, 150 066, 2015.

Gamble, D. W., Parnell, D. B., and Curtis, S.: Spatial variability of the Caribbean mid-summer drought and relation to north Atlantic high circulation, International Journal of Climatology, 28, 343–350, 2008.

Gan, M., Kousky, V., and Ropelewski, C.: The South America monsoon circulation and its relationship to rainfall over west-central Brazil, Journal of climate, 17, 47–66, 2004.

Geil, K. L., Serra, Y. L., and Zeng, X.: Assessment of CMIP5 model simulations of the North American monsoon system, Journal of Climate,
470   26, 8787–8801, 2013.

Giannini, A., Saravanan, R., and Chang, P.: The preconditioning role of tropical Atlantic variability in the development of the ENSO teleconnection: Implications for the prediction of Nordeste rainfall, Climate Dynamics, 22, 839–855, 2004.

Harris, I., Jones, P. D., Osborn, T. J., and Lister, D. H.: Updated high-resolution grids of monthly climatic observations–the CRU TS3. 10 Dataset, International journal of climatology, 34, 623–642, 2014.

475   Herrera, E., Magaña, V., and Caetano, E.: Air–sea interactions and dynamical processes associated with the midsummer drought, International Journal of Climatology, 35, 1569–1578, 2015.

Huffman, G. J., Adler, R. F., Bolvin, D. T., and Nelkin, E. J.: The TRMM multi-satellite precipitation analysis (TMPA), in: Satellite rainfall applications for surface hydrology, pp. 3–22, Springer, 2010.

Jones, C. and Carvalho, L. M.: Active and break phases in the South American monsoon system, Journal of Climate, 15, 905–914, 2002.

480   Jones, C. and Carvalho, L. M.: Climate change in the South American monsoon system: present climate and CMIP5 projections, Journal of Climate, 26, 6660–6678, 2013.

Kennedy, J., Rayner, N., Smith, R., Parker, D., and Saunby, M.: Reassessing biases and other uncertainties in sea surface temperature observations measured in situ since 1850: 2. Biases and homogenization, Journal of Geophysical Research: Atmospheres, 116, 2011.

Lahmers, T. M., Castro, C. L., Adams, D. K., Serra, Y. L., Brost, J. J., and Luong, T.: Long-term changes in the climatology of transient
485   inverted troughs over the North American monsoon region and their effects on precipitation, Journal of Climate, 29, 6037–6064, 2016.

Lee, J.-E., Lintner, B. R., Boyce, C. K., and Lawrence, P. J.: Land use change exacerbates tropical South American drought by sea surface temperature variability, Geophysical Research Letters, 38, 2011.

Magaña, V., Amador, J. A., and Medina, S.: The midsummer drought over Mexico and Central America, Journal of Climate, 12, 1577–1588, 1999.

490   Marengo, J. A., Liebmann, B., Kousky, V. E., Filizola, N. P., and Wainer, I. C.: Onset and end of the rainy season in the Brazilian Amazon Basin, Journal of Climate, 14, 833–852, 2001.

Marengo, J. A., Liebmann, B., Grimm, A. M., Misra, V., Silva Dias, P. L., Cavalcanti, I. F. A., Carvalho, L. M. V., Berbery, E. H., Ambrizzi, T., Vera, C. S., Saulo, A. C., Nogues-Paegle, J., Zipser, E., Seth, A., and Alves, L. M.: Recent developments on the South American monsoon system, International Journal of Climatology, 32, 1–21, 2012.

495   Menary, M. B., Kuhlbrodt, T., Ridley, J., Andrews, M. B., Dimdore-Miles, O. B., Deshayes, J., Eade, R., Gray, L., Ineson, S., Mignot, J., Roberts, C. D., Robson, J., Wood, R. A., and Xavier, P.: Preindustrial Control Simulations With HadGEM3-GC3. 1 for CMIP6, Journal of Advances in Modeling Earth Systems, 10, 3049–3075, 2018.

Mulcahy, J. P., Jones, C., Sellar, A., Johnson, B., Boutle, I. A., Jones, A., Andrews, T., Rumbold, S. T., Mollard, J., Bellouin, N., Johnson, C. E., Williams, K. D., Grosvenor, D. P., and McCoy, D. T.: Improved aerosol processes and effective radiative forcing in HadGEM3 and
500   UKESM1, Journal of Advances in Modeling Earth Systems, 10, 2786–2805, 2018.

Nieto-Ferreira, R. and Rickenbach, T. M.: Regionality of monsoon onset in South America: a three-stage conceptual model, International Journal of Climatology, 31, 1309–1321, 2011.

Ordoñez, P., Nieto, R., Gimeno, L., Ribera, P., Gallego, D., Ochoa-Moya, C. A., and Quintanar, A. I.: Climatological moisture sources for the Western North American Monsoon through a Lagrangian approach: their influence on precipitation intensity, Earth System Dynamics, 10, 59–72, 2019.

505

Pascale, S. and Bordoni, S.: Tropical and extratropical controls of Gulf of California surges and summertime precipitation over the southwestern United States, Monthly Weather Review, 144, 2695–2718, 2016.

Pascale, S., Bordoni, S., Kapnick, S. B., Vecchi, G. A., Jia, L., Delworth, T. L., Underwood, S., and Anderson, W.: The impact of horizontal resolution on North American monsoon Gulf of California moisture surges in a suite of coupled global climate models, Journal of Climate, 29, 7911–7936, 2016.

510

Pascale, S., Carvalho, L. M., Adams, D. K., Castro, C. L., and Cavalcanti, I. F.: Current and Future Variations of the Monsoons of the Americas in a Warming Climate, Current Climate Change Reports, pp. 1–20, 2019.

Ryu, J.-H. and Hayhoe, K.: Understanding the sources of Caribbean precipitation biases in CMIP3 and CMIP5 simulations, Climate dynamics, 42, 3233–3252, 2014.

515

Seager, R. and Vecchi, G. A.: Greenhouse warming and the 21st century hydroclimate of southwestern North America, Proceedings of the National Academy of Sciences, 107, 21 277–21 282, 2010.

Seastrand, S., Serra, Y., Castro, C., and Ritchie, E.: The dominant synoptic-scale modes of North American monsoon precipitation, International Journal of Climatology, 35, 2019–2032, 2015.

Sellar, A. A., Jones, C. G., Mulcahy, J., Tang, Y., Yool, A., Wiltshire, A., O'Connor, F. M., Stringer, M., Hill, R., Palmieri, J., Wood-

520

ward, S., de Mora, L., Kuhlbrodt, T., Rumbold, S., Kelley, D. I., Ellis, R., Johnson, C. E., Walton, J., Abraham, N. L., Andrews, M. B., Andrews, T., Archibald, A. T., Berthou, S., Burke, E., Blockley, E., Carslaw, K., Dalvi, M., Edwards, J., Folberth, G. A., Gedney, N., Griffiths, P. T., Harper, A. B., Hendry, M. A., Hewitt, A. J., Johnson, B., Jones, A., Jones, C. D., Keeble, J., Liddicoat, S., Morgenstern, O., Parker, R. J., Predoi, V., Robertson, E., Siahaan, A., Smith, R. S., Swaminathan, R., Woodhouse, M. T., Zeng, G., and Zerroukat, M.: UKESM1: Description and evaluation of the UK Earth System Model, Journal of Advances in Modeling Earth Systems, 0,

525

https://doi.org/10.1029/2019MS001739, https://agupubs.onlinelibrary.wiley.com/doi/abs/10.1029/2019MS001739, 2019.

Sheffield, J., Barrett, A. P., Colle, B., Nelun Fernando, D., Fu, R., Geil, K. L., Hu, Q., Kinter, J., Kumar, S., Langenbrunner, B., Lombardo, K., Long, L. N., Maloney, E., Mariotti, A., Meyerson, J. E., Mo, K. C., David Neelin, J., Nigam, S., Pan, Z., Ren, T., Ruiz-Barradas, A., Serra, Y. L., Seth, A., Thibeault, J. M., Stroeve, J. C., Yang, Z., and Yin, L.: North American climate in CMIP5 experiments. Part I: Evaluation of historical simulations of continental and regional climatology, Journal of Climate, 26, 9209–9245, 2013a.

530

Stensrud, D. J., Gall, R. L., and Nordquist, M. K.: Surges over the Gulf of California during the Mexican monsoon, Monthly Weather Review, 125, 417–437, 1997.

Trenberth, K. E.: The definition of El Nino, Bulletin of the American Meteorological Society, 78, 2771–2778, 1997.

Trenberth, K. E., Branstator, G. W., Karoly, D., Kumar, A., Lau, N.-C., and Ropelewski, C.: Progress during TOGA in understanding and modeling global teleconnections associated with tropical sea surface temperatures, Journal of Geophysical Research: Oceans, 103,

535

14 291–14 324, 1998.

Turrent, C. and Cavazos, T.: Role of the land-sea thermal contrast in the interannual modulation of the North American Monsoon, Geophysical Research Letters, 36, 2009.

Vera, C. and Silvestri, G.: Precipitation interannual variability in South America from the WCRP-CMIP3 multi-model dataset, Climate dynamics, 32, 1003–1014, 2009.

540   Vera, C., Higgins, W., Amador, J., Ambrizzi, T., Garreaud, R., Gochis, D., Gutzler, D., Lettenmaier, D., Marengo, J., Mechoso, C. R., Nogues-Paegle, J., Dias, P. L. S., and Zhang, C.: Toward a unified view of the American monsoon systems, Journal of Climate, 19, 4977–5000, 2006.

Wang, P. X., Wang, B., Cheng, H., Fasullo, J., Guo, Z., Kiefer, T., and Liu, Z.: The global monsoon across time scales: Mechanisms and outstanding issues, Earth-Science Reviews, 174, 84–121, 2017.

545   Williams, K. D., Copsey, D., Blockley, E. W., Bodas-Salcedo, A., Calvert, D., Comer, R., Davis, P., Graham, T., Hewitt, H. T., Hill, R., Hyder, P., Ineson, S., Johns, T. C., Keen, A. B., Lee, R. W., Megann, A., Milton, S. F., Rae, J. G. L., Roberts, M. J., Scaife, A. A., Schiemann, R., Storkey, D., Thorpe, L., Watterson, I. G., Walters, D. N., West, A., Wood, R. A., Woollings, T., and Xavier, P. K.: The Met Office global coupled model 3.0 and 3.1 (GC3. 0 and GC3. 1) configurations, Journal of Advances in Modeling Earth Systems, 10, 357–380, 2018.

Yin, L., Fu, R., Shevliakova, E., and Dickinson, R. E.: How well can CMIP5 simulate precipitation and its controlling processes over tropical
550   South America?, Climate Dynamics, 41, 3127–3143, 2013.

Zhou, T., Turner, A. G., Kinter, J. L., Wang, B., Qian, Y., Chen, X., Wu, B., Liu, B., Zou, L., and Bian, H.: GMMIP (v1. 0) contribution to CMIP6: global monsoons model inter-comparison project, Geoscientific Model Development, 9, 3589–3604, 2016.